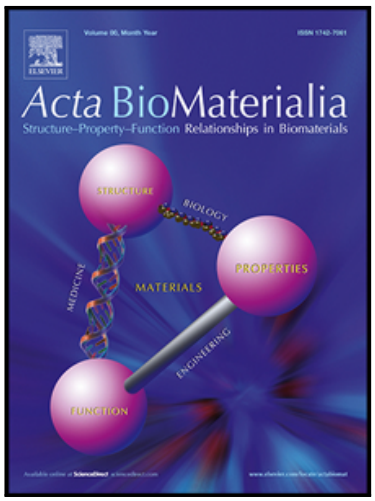

The elasto-plastic nano- and microscale compressive behaviour of rehydrated mineralised collagen fibres

Alexander Groetsch , Aurélien Gourrier , Daniele Casari , Jakob Schwiedrzik , Jonathan D. Shephard , Johann Michler , Philippe K. Zysset , Uwe Wolfram

PII: S1742-7061(23)00184-8
DOI: https://doi.org/10.1016/j.actbio.2023.03.041
Reference: ACTBIO 8670

To appear in: *Acta Biomaterialia*

Received date: 18 August 2022
Revised date: 13 March 2023
Accepted date: 27 March 2023

Please cite this article as: Alexander Groetsch , Aurélien Gourrier , Daniele Casari , Jakob Schwiedrzik , Jonathan D. Shephard , Johann Michler , Philippe K. Zysset , Uwe Wolfram , The elasto-plastic nano- and microscale compressive behaviour of rehydrated mineralised collagen fibres, *Acta Biomaterialia* (2023), doi: https://doi.org/10.1016/j.actbio.2023.03.041

The elasto-plastic nano- and microscale compressive behaviour of rehydrated mineralised collagen fibres

Alexander Groetsch[a,‡], Aurélien Gourrier[b], Daniele Casari[c], Jakob Schwiedrzik[c], Jonathan D. Shephard[d], Johann Michler[c], Philippe K. Zysset[e], Uwe Wolfram[a*]

[a]Institute of Mechanical, Process & Energy Engineering, School of Engineering & Physical Sciences, Heriot-Watt University, Edinburgh, UK

[b]Univ. Grenoble Alpes, CNRS, LIPhy, 38000 Grenoble, France

[c]Empa, Swiss Federal Laboratories for Materials Science and Technology, Thun, Switzerland

[d]Institute of Photonics and Quantum Sciences, School of Engineering and Physical Sciences, Heriot-Watt University, Edinburgh, UK

[e]ARTORG Centre for Biomedical Engineering Research, University of Bern, Switzerland

[*]Corresponding author's contact details: u.wolfram@hw.ac.uk, Heriot-Watt University, Edinburgh, EH14 4AS, UK

[‡]Current address: Empa, Swiss Federal Laboratories for Materials Science and Technology, Thun, Switzerland

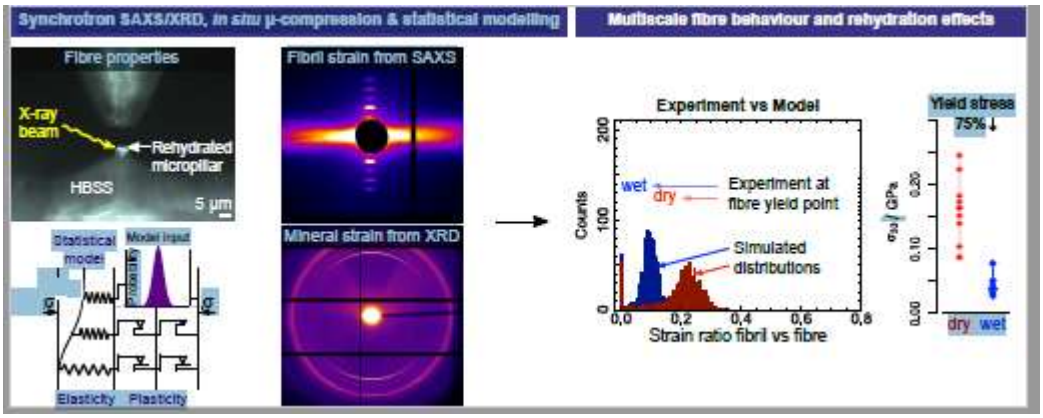

Abstract

The hierarchical design of bio-based nanostructured materials such as bone enables them to combine unique structure-mechanical properties. As one of its main components, water plays an important role in bone's material multiscale mechanical interplay. However, its influence has not been quantified at the length-scale of a mineralised collagen fibre. Here, we couple *in situ* micropillar compression, and simultaneous synchrotron small angle X-ray scattering (SAXS) and X-ray diffraction (XRD) with a statistical constitutive model. Since the synchrotron data contain statistical information on the nanostructure, we establish a direct connection between experiment and model to identify the rehydrated elasto-plastic micro- and nanomechanical fibre behaviour. Rehydration led to a decrease of 65%-75% in fibre yield stress and compressive strength, and 70% in stiffness with a 3x higher effect on stresses than strains. While in agreement with bone extracellular matrix, the decrease is 1.5-3x higher compared to micro-indentation and macro-compression. Hydration influences mineral more than fibril strain with the highest difference to the macroscale when comparing mineral and tissue levels. The effect of hydration seems to be strongly mediated by ultrastructural interfaces while results provide insights towards mechanical consequences of reported water-mediated structuring of bone apatite. The missing reinforcing capacity of surrounding tissue for an excised fibril array is more pronounced in wet than dry conditions, mainly related to fibril swelling. Differences leading to higher compressive strength between mineralised tissues seem not to depend on rehydration while the lack of kink bands supports the role of water as an elastic embedding influencing energy-absorption mechanisms.

Statement of significance: Characterising structure-property-function relationships in hierarchical biological materials helps us to elucidate mechanisms that enable their unique properties. Experimental and computational methods can advance our understanding of their complex behaviour with the potential to inform bio-inspired material development. In this study, we close a gap for bone's fundamental mechanical building block at micro- and nanometre length scales. We establish a direct connection between experiments and simulations by coupling *in situ* synchrotron tests with a statistical model and quantify the behaviour of rehydrated single mineralised collagen fibres. Results suggest a high influence of hydration on structural interfaces, and the role of water as an elastic embedding by outlining important differences between wet and dry elasto-plastic properties of mineral nanocrystals, fibrils and fibres.

Keywords

Mineralised collagen fibre, Rehydration, Nano- and micromechanics, *In situ* synchrotron SAXS/XRD, Micropillar compression, Strength and failure, Statistical elasto-plastic constitutive model

1 Introduction

The intriguing architecture of bone determines its remarkable ability to combine mechanical properties that are commonly mutually exclusive. While being a light-weight material, it combines high toughness and high strength [1–4] via an elaborate design of its organic and inorganic constituents [5, 6]. Studying bone on its multiple length scales enables us to understand the underlying deformation mechanisms. For bone-related diseases this detailed knowledge is essential to elucidate the related changes in bone's architecture, especially for pathologies such as osteogenesis imperfecta (OI) where the increased brittleness is related to changes at the molecular level [7]. Thus, not only the information on the bone quantity but also on the micro- and ultrastructure is important. For bio-inspired materials deciphering the structure-mechanical function relationships can inspire new designs including nanostructured metamaterials while identifying potential candidate materials for bone implants [6, 8–12]. In digital healthcare, computational models have the potential to improve diagnosis and treatment strategies [13–16]. They can be used to simulate bone's mechanical behaviour under multiple loading conditions and to predict its failure behaviour. Such models, however, critically depend on the underlying material description on bone's multiple length scales [17–21].

Since bone is a multiscale material, different mechanical properties and governing deformation mechanisms are present at its different architectural levels [5, 6, 9, 22–24]. This includes scale transitions with superior strength at the bone extracellular matrix level compared to the macroscopic tissue level [25, 26]. While there is substantial information at the macroscale, there is limited knowledge on ultimate properties such as strength and ultimate strain at the micro- and nanometre length scale that might explain these scale transitions [27]. This is in part due to the challenges imposed on *in situ* experiments to extract micro- and nanoscale structure-property relationships of bone's main constituents, collagen, mineral, and water. At the micro- and nanoscale, bone's elementary mechanical units are the mineralised collagen fibre and mineralised collagen fibril [9, 23, 28, 29]. A mineralised collagen fibre represents an array of mineralised collagen fibrils [5, 6, 23, 30] which consists of type I collagen molecules and mineral particles of primarily carbonated hydroxyapatite [31, 32]. The fibrils are embedded in an extrafibrillar matrix that consists of a layer of non-collagenous proteins, proteoglycans, extrafibrillar mineral and water [33–37] while sacrificial bonds, cross-links and dilatational bands represent important toughening mechanisms along the scales [36, 38–41]. The collagen molecules within the mineralised collagen fibrils show a staggered arrangement. The intrafibrillar mineral particles are located within the gap zones of these molecules [31, 32, 42–44].

Water makes up about 14-20 wt% of bone [45, 46]. It is reported that the hydration state has an influence on the mechanical properties at the material's different hierarchical levels as seen in experiments and simulations [47–51]. At the extracellular matrix level, yield stress and compressive strength are reduced by 60% to 75% for rehydrated samples [50]. Bone tissue shows a ductile behaviour at this length scale, also in dry conditions, and a transition to quasi-brittle behaviour at the organ level [25]. For millimetre sized bone samples, hydration leads to a more ductile behaviour [49].

Micropillars from ovine bone extracellular matrix have been tested under quasi-physiologic conditions and confirmed the ductile behaviour on these small length scales [50]. Furthermore, tension and compression of millimetre sized bone samples were combined with SAXS and WAXS/XRD measurements under dry and wet conditions [49, 52, 53]. A reduction of elastic bulk properties was reported as well as a decrease in the ratios between fibril, mineral and macroscopic strains. Water can be found in different regions of the bone matrix influencing the mineral-organic matrix interactions [46, 54]. Apart from pore spaces such as lacunae, canaliculi, and Haversian channels, water is present in a bound form in carbonated apatite as well as in the extracellular bone matrix [46, 47, 54] and small gap regions [55]. It is also present as surface water around mineralised collagen fibrils and mineral platelets which is discussed to affect the energy dissipation [46, 54], thus, influencing mechanisms at the extracellular matrix level. It is further postulated that dehydration of the nanocomposite bone has different effects on mineral and collagen, which, in turn, leads to changes in the overall tissue behaviour [47]. However, a crucial gap still exits. The micro- and nanomechanical behaviour of a mineralised collagen fibre under rehydrated conditions has not been studied so far.

Consequently, this study aims at (i) performing micro- and nanomechanical testing of rehydrated mineralised collagen fibres, (ii) quantifying the influence of hydration at the level of a mineralised collagen fibre, mineralised collagen fibrils and mineral nanocrystals, and (iii) using an existing statistical constitutive model as an evaluation method to identify hydrated mechanical fibre properties at molecular and fibrillar levels, thus, capturing the material behaviour.

2 Materials and methods

Recently, we reported results on the micro- and nanometre length scale compressive behaviour of single mineralised collagen fibres [21, 56]. Micropillar compression [25, 57] and synchrotron radiation X-ray scattering and diffraction techniques (SAXS/XRD) [42, 58–65] were used to extract the mechanical behaviour of a mineralised collagen fibre and the interplay with its mechanical components under dry conditions. Combined with ultrastructural data, those findings were used to develop a statistical elasto-plastic model that explains the micro- and nanoscale fibre behaviour [21]. The extension towards a setup with rehydrated samples now lets us deduce the fibre mechanical properties close to their hydration state in a combined experimental and computational approach.

2.1 SAXS/XRD with micropillar compression under rehydrated conditions

Dissection, ultra-milling, laser machining and focused ion beam milling (FIB) were used to separate micropillars from individual mineralised collagen fibres for mechanical testing using a previously developed protocol [56]. To ensure comparability, micropillars were extracted from the same ten turkey legs as used for the dry testing with samples being stored at -22°C in between both synchrotron campaigns [56]. Briefly, dissection methods using a scalpel and a diamond band saw (Exakt, Norderstedt, Reichert-Jung) were used to separate naturally highly mineralised tendon pieces

from turkey legs (*tarsometatarsus*). Mineralised turkey leg tendon (MTLT) is an established model system for bone due to its uniaxial fibre arrangement and similar structural set-up at the mineralised collagen

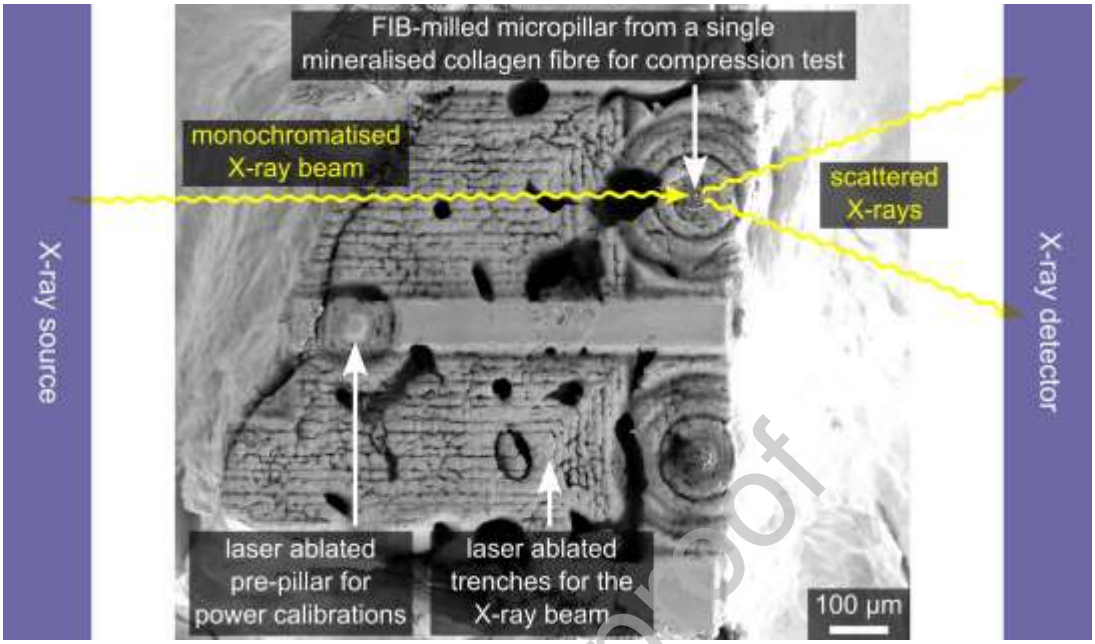

Figure 1: Sample geometry for simultaneous micropillar compression and SAXS/XRD. The SEM image shows the top view of laser ablated trenches to allow the X-ray beam to pass through to FIB-milled micropillars, which were extracted from individual mineralised collagen fibres. They were compressed while SAXS or XRD patterns were taken in a synchrotron setup to quantify the fibril and mineral strain while the apparent fibre behaviour was measured by an integrated microindenter (Figure 2). To account for different tissue reactions during laser processing (natural variability), a pre-test pre-pillar was ablated, checked with focus variation microscopy, and the laser power was adjusted if necessary.

fibre level [17, 34, 42, 43, 66–69]. Samples were kept frozen at -22°C until preparation. Before dissection, samples were thawed, covered in phosphate buffered saline solution (PBSS). Tendon pieces of 1.5 mm in diameter and 10.0 mm in length were glued into cylindrical aluminium sample holders using a 2-component epoxy resin adhesive (Schnellfest, UHU, Germany). The free end was polished with an ultramiller (Polycut E, Reichert-Jung, Germany). Ultra-short (picosecond) pulsed laser ablation (TruMicro 5250-3C, Trumpf, Germany) was used to cut pre-pillars of 32.85 ± 0.91 µm, centred around a single mineralised collagen fibre (Figure 1). The plasma mediated ablation process minimised the thermal impact during manufacturing. Raman measurements and finite element analyses were used to confirm that the physio-chemical properties were not changed by the laser ablation, and that the ablation process did not exceed the denaturation temperature for dry collagen [56, 70]. Focused ion beam milling (Quanta 3D FEG, FEI, USA) was then used to cut the final micropillars. Final micropillars were 6.4 ± 0.6 µm in diameter and 2.05 ± 0.09 in aspect ratio. The possible effects of FIB induced Gallium implantation was assessed by means of Monte Carlo simulations using the software SRIM [71]. Affected layers were shown to be thinner than 30 nm and can, thus, be neglected compared to the micropillar mean diameter with respect to its influence on the mechanical behaviour [56, 72, 73]. To test micropillars from single mineralised collagen fibres in

combination with SAXS/XRD under conditions closer to their natural hydration state, a rehydration set-up was developed that allowed *in situ* micropillar compression experiments at a synchrotron beamline (Figure 2). Before mechanical testing, samples were rehydrated for 2 hours in Hank's balanced salt solution (HBSS) following

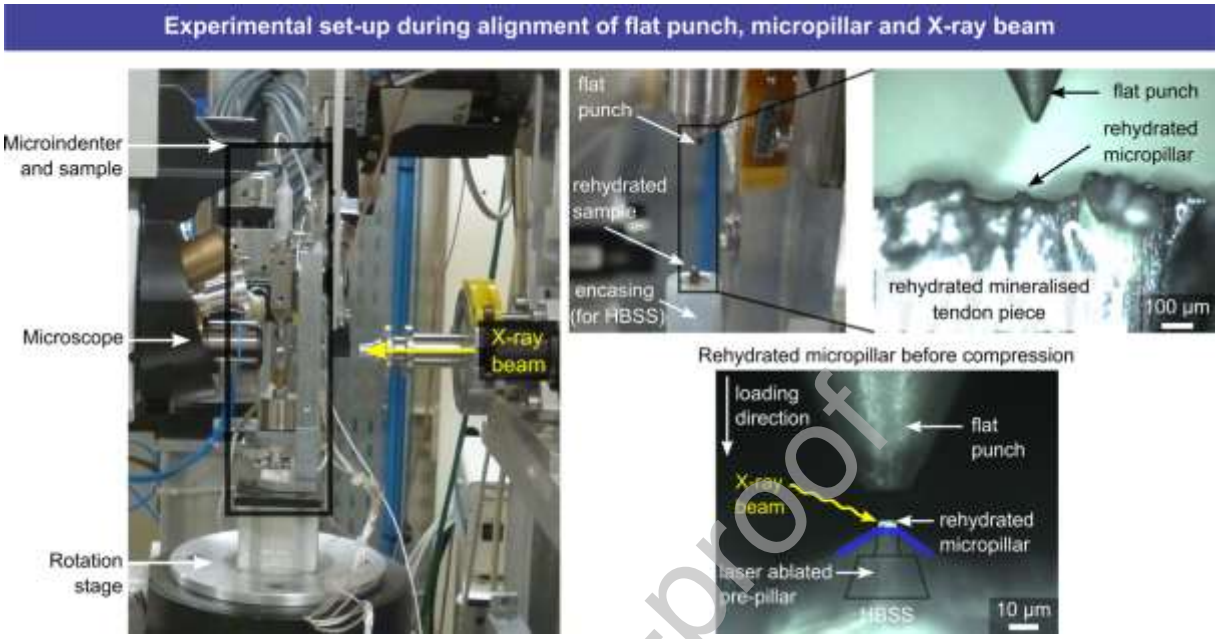

Figure 2: Experimental set-up for the simultaneous micropillar compression and SAXS/XRD measurements of mineralised collagen fibres under rehydrated conditions. The microindenter was implemented into the X-ray set-up of the micro-focus beamline ID13 (ESRF) and placed on a rotation z-stage for the alignment between flat punch, micropillar and X-ray beam. An encasing for the reservoir of Hank's balanced salt solution (HBSS) was created by wrapping a paraffin-polyethylene foil (Parafilm) around the aluminium tube with the mineralised tendon piece. This reservoir was refilled at distinct intervals over a period of 2h before testing. The sample was kept rehydrated from the base during the test via diffusion. Bottom-right: The sample outline (black) is indicated and includes the laser ablated pre-pillar. The blue lines represent the average HBSS surface level during testing. HBSS rose at the micropillar due to surface tension. See [56] for details on the experimental setup under dry conditions.

previously established protocols used for bone extracellular matrix micropillars with the same dimensions [50]. The level of hydration was checked using an optical microscope and if necessary, HBSS was added using a pipette. For the alignment between micropillar, flat punch and X-ray beam, excessive HBSS was removed with a pipette so that the micropillar was visible with the microscope (Figure 2). During alignment, the sample was kept rehydrated via diffusion from the micropillar base by filling the HBSS reservoir (Parafilm encasing) at regular intervals. Before compression started, the HBSS level was checked with an optical microscope (Figure 2, bottom-right). We also confirmed that the sample surface was accessible, and the flat punch was free of HBSS during the tip approach. The sufficient hydration state was further checked in preliminary tests. These tests showed that 0.05 ml drops of water are not evaporated after 15 min at ambient temperature which is sufficient for the testing at the beamline. In addition, we used Darcy's law [74] in 1D to check whether an active diffusion wets the sample.

Mechanical testing and X-ray diffraction followed protocols used for dry tests [56]. Uniaxial micropillar compression experiments were performed with a custom-built microindenter (Alemnis AG, Switzerland) inside a small angle X-ray scattering (SAXS) and X-ray diffraction (XRD) set-up at the ID13 of the European Synchrotron Radiation Facility (ESRF) under the same beamline configuration as for our previous experiment on dry micropillars [56]. Micropillars were compressed until failure while being exposed to X-rays at 120 discrete time points. A quasi-static loading protocol at 5 nm/s was used until a mean maximum strain of 12% including partial unloading steps of 50 nm every 150 nm. Either SAXS- or XRD-patterns were recorded during the micropillar compression test to quantify strains of the mineralised collagen fibrils (calcified collagen phase) or mineral particles (mineral phase). X-ray exposure was every 5 s at an energy of E = 13.3 keV. Exposure time for SAXS acquisitions was 75 ms, for XRD 185 ms. The shutter was closed between acquisitions. The beamsize was 5.5 µm in vertical and 7.0 µm in horizontal direction. The beam was focused several micrometres below the top surface of the micropillar to avoid parasitic scattering from the diamond flat punch. A single-photon counting detector was used to capture the diffracted/scattered X-ray signal (Eiger, Dectris, Switzerland). Overall, these experimental parameters were the same as those used for dry micropillars to minimise the X-ray dose and to ensure a direct comparison between wet and dry samples.

2.2 SAXS/XRD and mechanical data analysis

Data analysis for the fibre properties was done in Python (Python Software Foundation, Python Language Reference, version 2.7) [75] and R [76]. Assuming a negligible volume change [77] and a uniaxial stress state within the micropillar [78], engineering stress σ_{eng} was calculated by dividing the force by the top surface micropillar area. Engineering strain ε_{eng} was calculated using the displacement and the micropillar height. Geometric measurements were taken with an SEM (Quanta 3D FEG, FEI, USA). Displacement data were frame-compliance and base-compliance corrected. For the base-compliance correction, a modified Sneddon approach [79, 80] was used to account for the elastic sink-in of the micropillar into the substrate beneath (elastic half-space) while considering a fillet radius at the bottom of the micropillar. Engineering stress-strain data were then converted to true stresses and strains via $\sigma_{33}=\sigma_{eng}(1+\varepsilon_{eng})$ and $\ln(U_{33}) = \ln(1+\varepsilon_{eng})$ following previously reported procedures [25, 56, 78] (Figure 3, bottom right). An envelope was fitted to the stress strain curves using a cubic spline with the inflection points of the loading and unloading segments as nodes. This envelope was used to determine the apparent mechanical properties at the mineralised collagen fibre level. Fibre yield values were extracted based on the 0.2% offset criterion, compressive strength and ultimate strain at the maximum of the envelope. Unloading moduli were calculated via linear regression of the unloading segments and their reduction served to estimate damage. The last unloading modulus before the yield point was defined as the apparent Young's modulus (Figure 3).

The deformation of mineralised collagen fibrils and mineral particles can be assessed by analysing changes of the SAXS- or XRD-patterns as a result of the compression. For the SAXS pattern, changes in the Bragg-peaks are related to the changes in the axial arrangement of the intrafibrillar collagen

molecules (d period spacing), partly filled with mineral nanocrystals [56, 61]. For the XRD pattern, deformation of the mineral nanocrystals is quantified by tracking changes of the 002 reflection representing changes of a crystal plane perpendicular to the particle c-axis and, thus, to its longitudinal direction. Both the SAXS meridional reflections and the c-axis of the mineral nanocrystals are aligned along the longitudinal direction of the mineralised collagen fibre (Figure 3, top). This allows it to directly compare strain values at fibre-, fibril- and mineral-levels when micropillar compression is combined

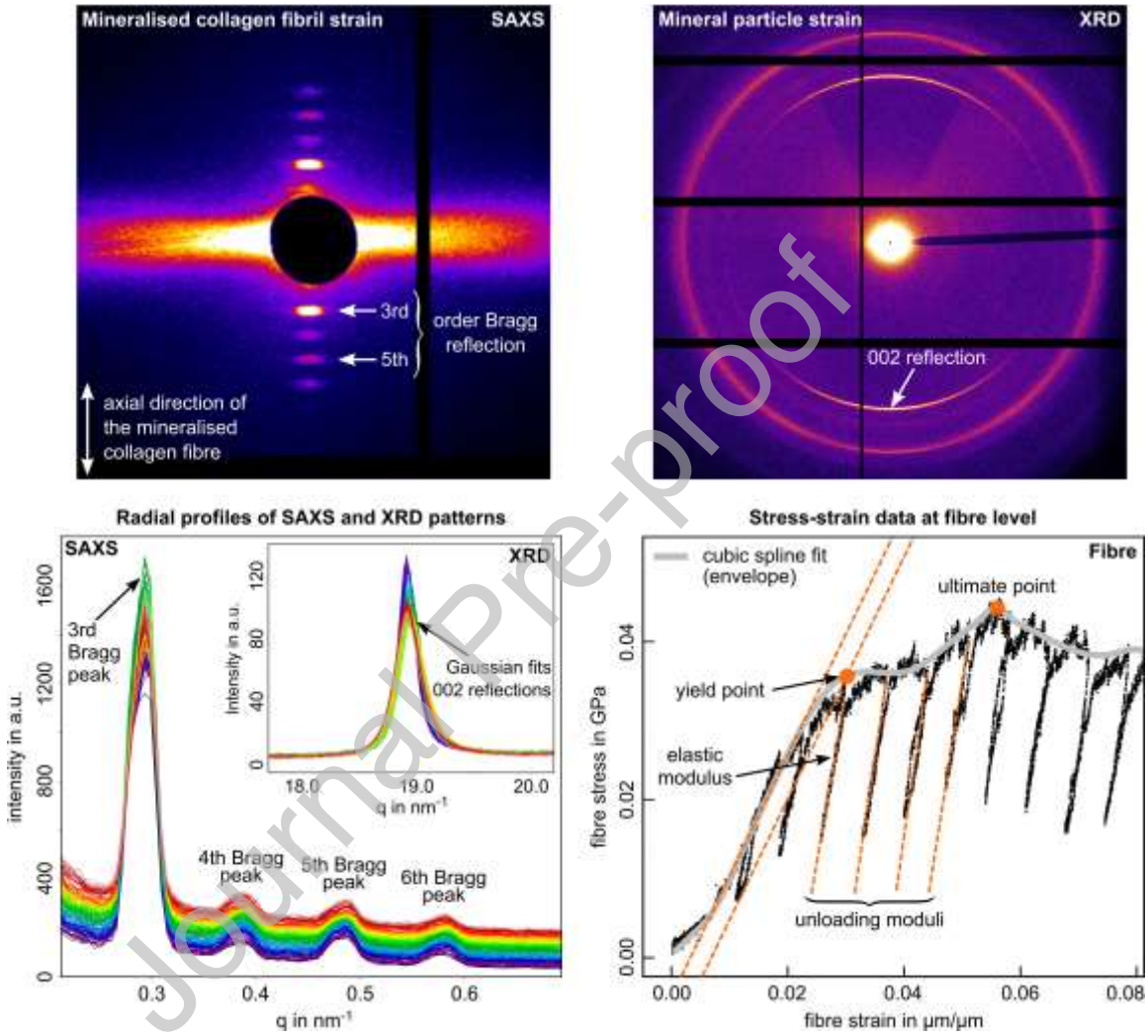

Figure 3: SAXS and XRD patterns as well as data analysis at mineral-, fibril- and fibre-levels. Top-left: SAXS reflections where the 3rd and 5th Bragg order peak were used to determine the mineral collagen fibril strain; Top-right: XRD reflections where the 002 Bragg peak was used to determine the mineral particle strain; Bottom left: Radial profiles from SAXS and XRD reflections to analyse changes in the position of the wave vector *q* resulting from compressing the fibre micropillar. Peak positions were identified via a Gaussian fit for every of the 120 X-ray acquisitions points per sample. The background (diffuse and parasitic scattering) was fitted with a first order polynomial. The resulting wave vector values *q* were then converted to *d*-values via the relation $q = 2\pi/d$. A detailed description of the X-ray data analysis can be found in [56]; Bottom-right: Apparent mechanical properties at the mineralised collagen fibre level were determined from apparent stress-strain curves. A cubic spline (envelope) was fitted to the data using the inflection points as nods. This envelope was used to identify yield values based on the 0.2% offset criterion and ultimate values at the envelope's maximum. Unloading moduli represent the apparent fibre moduli with the last before the yield point defined as the apparent Young's modulus.

with SAXS and XRD measurements. Calibration measurements to determine the beam centre, sample-to-detector distance and tilt angle were done using silver behanate (SAXS) and di-aluminium dioxide (XRD). Data analysis for the SAXS and XRD patterns was done with a Python based custom-written software called 'pySXIm' (courtesy of Aurélien Gourrier, Université Grenoble Alpes, LIPhy, France; converted for Linux by Alexander Groetsch), and the ESRF-developed software Fit2d [81]. Both PCs for the mechanical testing and X-ray acquisition were integrated into the same computer network to synchronise the datasets for the analysis using the time stamps of the data log files. In total, 120 acquisition points were accessible throughout the compressive loading and data subsets from the fibre-, fibril- and mineral levels were identified for the strain ratio calculations [56]. The overall strain ratios in the elastic region between the fibre, fibril and mineral deformations were determined at the steepest slope of the cubic spline fit in the elastic region of the mineral-vs-fibre-strain and fibril-vs-fibre-strain plots (Figure S1 in Supplementary Material). Elastic regions were identified based on the previous analysis of the apparent fibre mechanical properties (Figure 3).

2.3 Constitutive model as a statistical evaluation tool for the biomaterial behaviour

The connection between the apparent mechanical properties at the mineralised collagen fibre level (microscale) and the deformation of the fibre components (nanoscale) was quantified based on comparing the strain of the mineral particles, the mineralised collagen fibrils and the mineralised collagen fibre [21, 56]. We have developed a constitutive model [21] to interpret such experiments and to quantify the compressive behaviour via those strain ratios. The model is necessary to account for experimental artefacts, which then allows us to simulate the micro- and nanomechanical behaviour of a mineralised collagen fibre, and to deduce its mechanical properties. It operates at the continuum-, molecular- and crystalline levels covering the fibre, fibrils, collagen molecules and mineral nanocrystals. Material properties for the model follow a statistical normal distribution to account for the microscale and naturally occurring heterogeneities in the material behaviour (Table 1). We previously showed that the use of a normal distribution is well suited to describe the heterogeneity of the biological material system [21]. Two nested shear lag models are used to calculate elastic properties at the fibre- and fibril level while two inelastic strain mechanisms capture the plasticity simulating the two interfaces in the intra- and extrafibrillar phases of mineral-collagen-mineral, and fibril-matrix-fibril. A parallel arrangement of several model elements represents the parallel array of fibrils within a fibre. The model outputs strain ratio distributions between the constitutive phases and the apparent fibre strain to allow a direct comparison to the statistical values from synchrotron experiments as a mean from the illuminated volume. In the model, we included a non-linear gradual recruitment of mineralised collagen fibrils, which was informed by ultrastructural data from synchrotron phase-contrast nanoCT scans [21], and which accounted for an experimental artefact. The high agreement between model and experiment [21] allows us to interpret the test results under rehydrated conditions.

We include hydration by adapting collagen stiffness [47, 82, 83] and the overall experimentally determined apparent yield strain ε_{33}^{yield} and related parameters (fibril and EFM yield strains) [21]

compared to the dry tested micropillars [56]. Thus, a reduced value for the modulus of collagen molecules of 0.9 GPa was used as a literature mean (Table 1), compared to 1.42 GPa for the dry fibre model [21]. For the formulation of our model, it was further assumed that the fibril volume fraction was kept constant. A full overview of model input parameters is given in Table 1 . By combining the knowledge from the experiments and the use of the model we can then derive the actual mechanical properties at the micro- and nanometre length scale including the stiffness of a mineralised collagen fibril. A more detailed description of the statistical constitutive model can be found in our previous work [21].

Table 1: Properties for the quasi-physiologic micro- and nanomechanical behaviour of a mineralised collagen fibre. The table lists the compositional parameters of the fibre (first section) to calculate fibril and fibre elasticity (second section) via two nested shear lag models. All the mineral is assumed to be located inside the fibril/provided as a mineral coating around the fibrils. Plasticity calculations were done based on the elasto-plastic rheological elements (third section). The number of rheological elements equals the number of fibrils. Own experimental values were taken where possible and referenced to the corresponding sections. Additional values were taken from the literature. See [21] for further details.

Model parameter	Variable	Value	Std	Source	Usage
Fibril volume fraction in fibre	ϕ_{mc}	0.86	-	[21]	Compositional parameters
Number of fibrils	n_{ele}	618	-	[21]	
Mineral volume fraction	ϕ_{min}	0.29	-	[17, 69, 99–101]	
NCP volume fraction	ϕ_{ncp}	0.14	-	[102]	
Fibril aspect ratio	γ_{fibril}	200	-	[5]	
Mineral particles aspect ratio	γ_{min}	25	-	[5, 95, 103, 104]	
Mineral Young's modulus	ϵ_{min}	114 GPa	15%	[5, 103, 105, 106]	
Collagen shear modulus	μ_{col}	0.9 GPa	15%	[5, 47, 82, 83, 105]	
EFM shear modulus	μ_{ef}	0.0002 GPa	15%	[17]	
Fibril Young's modulus	ϵ^{mc}	15.91 GPa	15%	calculated with shear lag model [21]	Elasticity
Fibre Young's modulus	ϵ	7.29 GPa	15%	calculated with shear lag model [21]	
Fibril yield strain	$\varepsilon^{y,mc}$	0.024	15%	[95, 107]	Plasticity
EFM yield strain	$\varepsilon^{y,ef}$	0.006	15%	using $\varepsilon^{y,mc}$, this study and series arrangement in model [21]	
Fibril hardening modulus	χ_{mc}	0.016 GPa	15%	0.1% of ϵ^{mc} [25]	
EFM hardening modulus	χ_{ef}	$0.05 \cdot 10^{-5}$ GPa	15%	0.1% of ϵ_{ef} (via μ_{ef}) [25]	
Fibril ultimate strain	$\varepsilon^{p,mc,ult}$	$\varepsilon^{p,mc,ult} \cdot 10^2$	15%	EFM failure assumed [50, 56, 108]	
EFM ultimate strain	$\varepsilon^{p,ef,ult}$	0.09	15%	this study with $\varepsilon^{p,mc,ult}$	

Std: standard deviation for statistically distributed mechanical properties; NCP: non-collageneous proteins (includes the volume fraction occupied by water when the tissue is wet); EFM: extrafibrillar matrix; mc: mineral-collagen composite (= mineralised collagen fibril); ef: extrafibrillar

2.4 SEM based failure mode analysis

Failure modes were analysed based on SEM images (E = 2 keV, tilt angle = 45° , Quanta 650 FEG SEM, FEI, USA). Samples were not re-sputtered for post-test failure analyses to avoid that features are being disguised. The micropillars are considered as fibril reinforced composites and failure mechanisms were categorised based on the classification scheme previously developed for dry testing [56]. This categorisation was derived from compressive failure modes and toughening mechanisms found in non-biological fibre-reinforced composites and bone tissue where more than one failure mechanism could be present in a single specimen.

2.5 Statistical analysis

Statistical analyses were done in R [84] and Python [85, 86]. Quantile-quantile plots and Shapiro-Wilk tests [87] were used to verify that the data were normally distributed and mean ± standard deviation were calculated. In addition, raw data of the samples by means of distribution independent median, minimum and maximum values are presented. To check for statistically significant differences between SAXS and XRD groups, and between the results from rehydrated and dry tests [56], a student t-test was used with a significance level of p=0.05.

3 Results

3.1 Mechanical properties at mineralised collagen fibre level and influence of hydration

In total, 14 micropillars were fabricated and 10 of the 14 rehydrated samples could be used for the analysis and the comparison to the dry testing. From the four remaining samples, two were used for pre-tests and two were lost due to technical difficulties. Data from rehydrated samples (5 SAXS, 5 XRD) were compared to those tested previously under dry conditions (6 SAXS, 5 XRD) [56]. No significant difference was found for the fibre mechanical properties between the SAXS and XRD group, and data were pooled for further analysis. Mean values for the experimental fibre mechanical properties are presented in Table 2 for yield stress σ_{33}^{yield}, yield strain ε_{33}^{yield}, compressive strength σ_{33}^{ult}, ultimate strain ε_{33}^{ult} and Young's modulus E_{fibre}. In addition, absolute values including median, minimum, and maximum are presented (Figure 4, left). No X-ray beam induced deterioration of the apparent material properties was found based on the unloading moduli (stiffness). No significant increase in damage, estimated as a reduction of the unloading moduli, was detected, up to a plastic strain of 10%. Hydration led to a three times higher reduction in stress than strain values. Due to hydration, a mean reduction of around 75% was observed for the yield stress σ_{33}^{yield} and compressive strength σ_{33}^{ult}. For the yield strain ε_{33}^{yield} and ultimate strain ε_{33}^{ult}, the rehydration led to a reduction of around 25%. The apparent Young's modulus E_{fibre} was reduced by 60-70%. All differences between results from the rehydrated and dry testing were significant (Tables 2 and 3).

Table 2: Apparent mechanical properties of a mineralised collagen fibre under rehydrated (N=10) and dry conditions (N=11). Results from dry micropillar compression tests from [56].

	σ_{33}^{yield} / GPa	ε_{33}^{yield}	σ_{33}^{ult} / GPa	ε_{33}^{ult}	ϵ_{fibre} / GPa
Wet	0.038 ± 0.015	0.030 ± 0.008	0.045 ± 0.018	0.044 ± 0.011	5.070 ± 1.155
Dry	0.154 ± 0.051	0.040 ± 0.011	0.180 ± 0.042	0.060 ± 0.016	16.472 ± 3.38

3.2 Mechanical properties of mineralised collagen fibrils and mineral particles with multiscale strain ratios and influence of hydration

Experiments and simulations show that the mineral strain is smaller compared to the fibril strain and the fibril strain smaller than the apparent fibre strain (Figure 4). Experimentally, this led to ratios in the elastic region of fibre:fibril:mineral of around 53:5:2. Mean values, thus, showed that only around 10% of strain is taken up by the mineralised collagen fibrils compared to the apparent fibre strain, and 4% by the mineral particles (Table 4). Mineral particle strain was on average 60% smaller than mineralised collagen fibril strain. The effect of hydration was nearly the same for the fibril-to-fibre and the mineral-to-fibre strain ratios with a difference of around 1%. For both the mineralised collagen fibrils and mineral particles, rehydration led to around 60% reduction of strain in the elastic region, with 59.5% for fibril-to-fibre, and 58.4% for mineral-to-fibre (Table 4 and Figure 6). These values are biased by the gradual recruitment of fibrils upon compression (Section 2.3 and [21]) (corrected simulation-based values are presented in the next paragraph and Table 5). Compared to the fibre:fibril:mineral ratios of 22:5:2 for dry testing [56], the experimental factor between the mineral and fibril strains remained the same with around 40% less strain taken up by the mineral particles compared to the mineralised collagen fibrils (dry: 0.39, wet: 0.40). Rehydration led to a significant difference of the mean fibril-to-fibre strain ratio from 0.23 to 0.10, and for the mean mineral-to-fibre strain ratio from 0.09 to 0.04, both measured in the elastic region (Section 3.2 and Table 4). Using the statistical model [21] (Section 2.3) to simulate the mineralised collagen fibre behaviour, we observe a fibre yield stress σ_{33}^{yield} of 0.040 GPa, a yield strain ε_{33}^{yield} of 0.029, a compressive strength of σ_{33}^{ult} of 0.044 GPa, and an apparent fibre modulus fibre of 7.026 GPa (Figure 5). With the shear lag model [21] (Section 2.3), we obtain a mineralised collagen fibril stiffness E_{fibril} of 15.921 GPa. Simulated mean values for the strain ratios at the yield point were 0.093 between fibrils and fibre as well as 0.035 between mineral nanocrystals and fibre. The ratio between mineral nanocrystals and fibrils was 0.376.

Comparing the mean values of fibre stiffness, yield stress and compressive strength as well as strain ratios between fibre, fibril and mineral, we observe an agreement of 88.8 ± 8.3 % between simulation results and experiments.

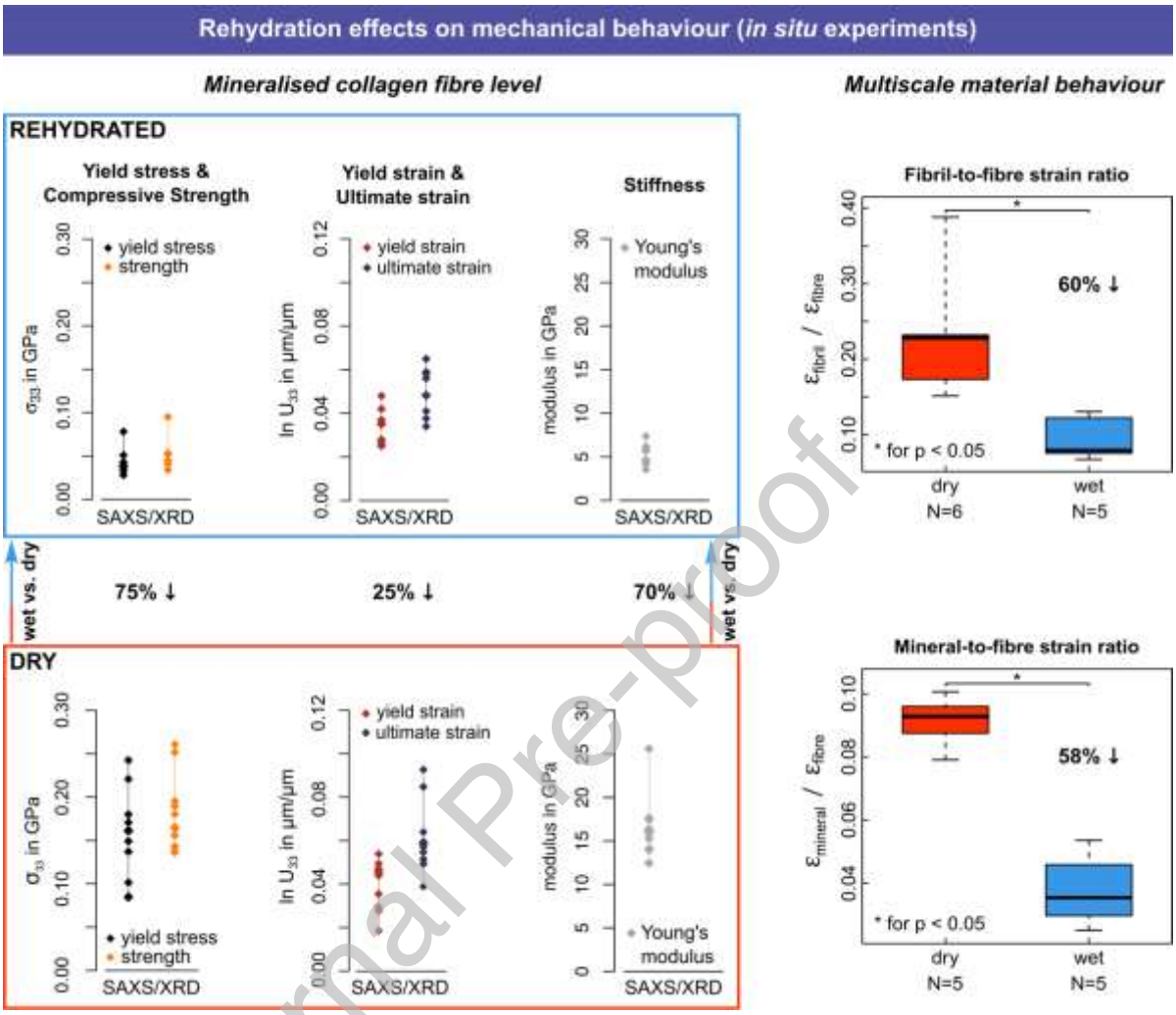

Figure 4: Experiment: Determined rehydration effects on the mechanical properties tested under dry (N=11) and rehydrated (N=10) conditions. Left: Effect at the apparent mineralised collagen level with minimum, median and maximum values for the apparent yield point, ultimate point and Young's modulus. Right: Multiscale strain ratios comparing values at fibre-, fibril- and mineral-levels. Dry testing results from [56].

Table 3: Comparison of rehydrated and dry testing results for the apparent mechanical properties at the mineralised collagen fibre level including p values.

	σ_{33}^{yield}	ε_{33}^{yield}	σ_{33}^{ult}	ε_{33}^{ult}	ϵ_{fibre}
Factor wet/dry compared to dry testing results [56]	0.247	0.744	0.251	0.741	0.308
p value	< 0.00001	0.032	< 0.00001	0.014	< 0.00001

Table 4: Experimental strain ratios (with fibril recruitment) (wet only) with factors between fibril and fibre as well as mineral and fibre under rehydrated and dry testing conditions determined in the elastic region. SAXS (N=5), XRD (N=5).

	$\varepsilon_{33}^{fibril}/\varepsilon_{33}^{fibre}$	$\varepsilon_{33}^{mineral}/\varepsilon_{33}^{fibre}$	$\varepsilon_{33}^{mineral}/\varepsilon_{33}^{fibril}$
Strain ratio (wet) (elastic region)	0.095 ± 0.029	0.038 ± 0.012	0.400 ± 0.021
Factor wet/dry (compared to dry testing results [56])	0.405	0.416	0.973
p value	0.004	< 0.0001	> 0.05

Thus, we can use the statistical constitutive model to exclude the gradual fibril recruitment, solve this experimental artefact, and derive the actual fibre behaviour (Figures 5 and 6). We then observe a mean fibril-to-fibre strain ratio of around 0.41, a mean mineral-to-fibre strain ratio of 0.13, and a mean mineral-to-fibril strain ratio of 0.32 at the moment the fibre yields (Figure 6). Under dry conditions, corresponding values are 0.70, 0.37 and 0.53, which led to ratios between wet and dry of 0.59, 0.35 and 0.60. Furthermore, a 12% higher hydration influence on the mineral than fibril strain was observed leading to a higher reduction in strain in the mineral phase (Table 5).

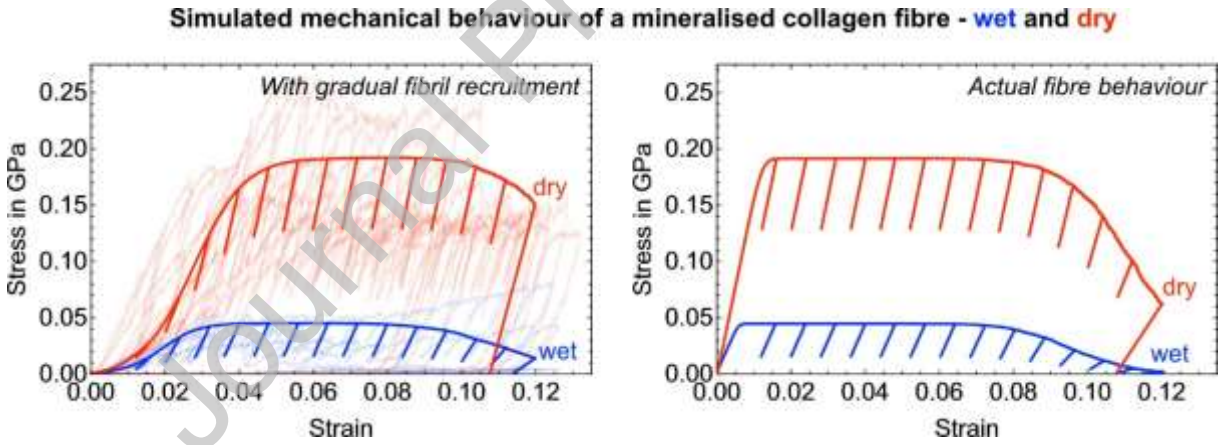

Figure 5: Model outcome at mineralised collagen fibre level for both wet and dry conditions. Left: With gradual fibril recruitment (see Section 2.3 and [21]). Experimental curves are shown in the background in faded red (from [56]) and blue. Right: Excluding the fibril recruitment and simulating the actual fibre behaviour.

3.3 SEM based failure mode analysis

For the majority of wet tested micropillars, mushrooming at the top surface was observed. In many cases, this was combined with microbuckling or fracture of mineralised collagen fibrils (Figure 7). The occurrence of mushrooming failure modes supports a homogeneous hydration state along the micropillar. If different hydration states would have been present, the lower end of the micropillar

would have been more compliant, and strain would localise there leading to failure at the bottom. Comparing failure modes in compressed micropillars under dry conditions [56] fibril-matrix interface

Table 5: Excluding fibril recruitment: Simulated strain ratios and factors between fibril and fibre as well as mineral and fibre under rehydrated and dry testing conditions determined at the numerical yield point.

	$\varepsilon_{33}^{fibril}/\varepsilon_{33}^{fibre}$	$\varepsilon_{33}^{mineral}/\varepsilon_{33}^{fibre}$	$\varepsilon_{33}^{mineral}/\varepsilon_{33}^{fibril}$
Strain ratio (wet) (at numerical yield)	0.41	0.13	0.32
Strain ratio (dry) (at numerical yield) [21]	0.70	0.37	0.53
Factor wet/dry	0.59	0.35	0.60

failure, axial splitting, fibril microbuckling and fibril fracture occurred in rehydrated and dry tested samples. Bulging and kink bands were only observed in dry tested micropillars, mushrooming only in rehydrated samples.

4 Discussion

We used a combination of multiscale experiment and statistical constitutive model to capture the micro- and nanomechanical behaviour of a mineralised collagen fibre close to their natural hydrated state. This included its apparent behaviour as well as the interplay with its components, mineralised collagen fibrils and mineral nanocrystals. To the best of our knowledge this is the first report on a combined experimental setup that integrates micropillar compression of rehydrated single mineralised collagen fibres with synchrotron small angle X-ray scattering (SAXS) and X-ray diffraction (XRD). Using our model as a statistical evaluation method [21] allowed it to account for experimental artefacts aiming to deduce the actual structure-mechanical properties of a single mineralised collagen fibre, and the dedicated effect that water has on the different constitutive phases. A direct comparison to experiments under dry conditions allowed us to quantify the effect of hydration on the multiscale material behaviour.

4.1 Apparent mechanical behaviour of rehydrated fibres and effect of hydration

Simulation results showed that the gradual fibril recruitment (experimental artefact) has a significant influence on both fibre yield values and the interaction between fibre constituents (Section 4.2 & Figure 6). Our results show that the mean apparent fibre Young's modulus is around 50% lower than wet micro-indentation moduli reported for mineralised turkey leg tendon [88]. Differences can be rationalised by the fact that the micro-indentation imprints were done on an array of mineralised collagen fibres covering the pore spaces in between fibres. The effect of hydration on these porosities, and the corresponding deformation and energy dissipation mechanisms might result in

different stiffness values compared to our results. We also have to consider the swelling and deformation of an

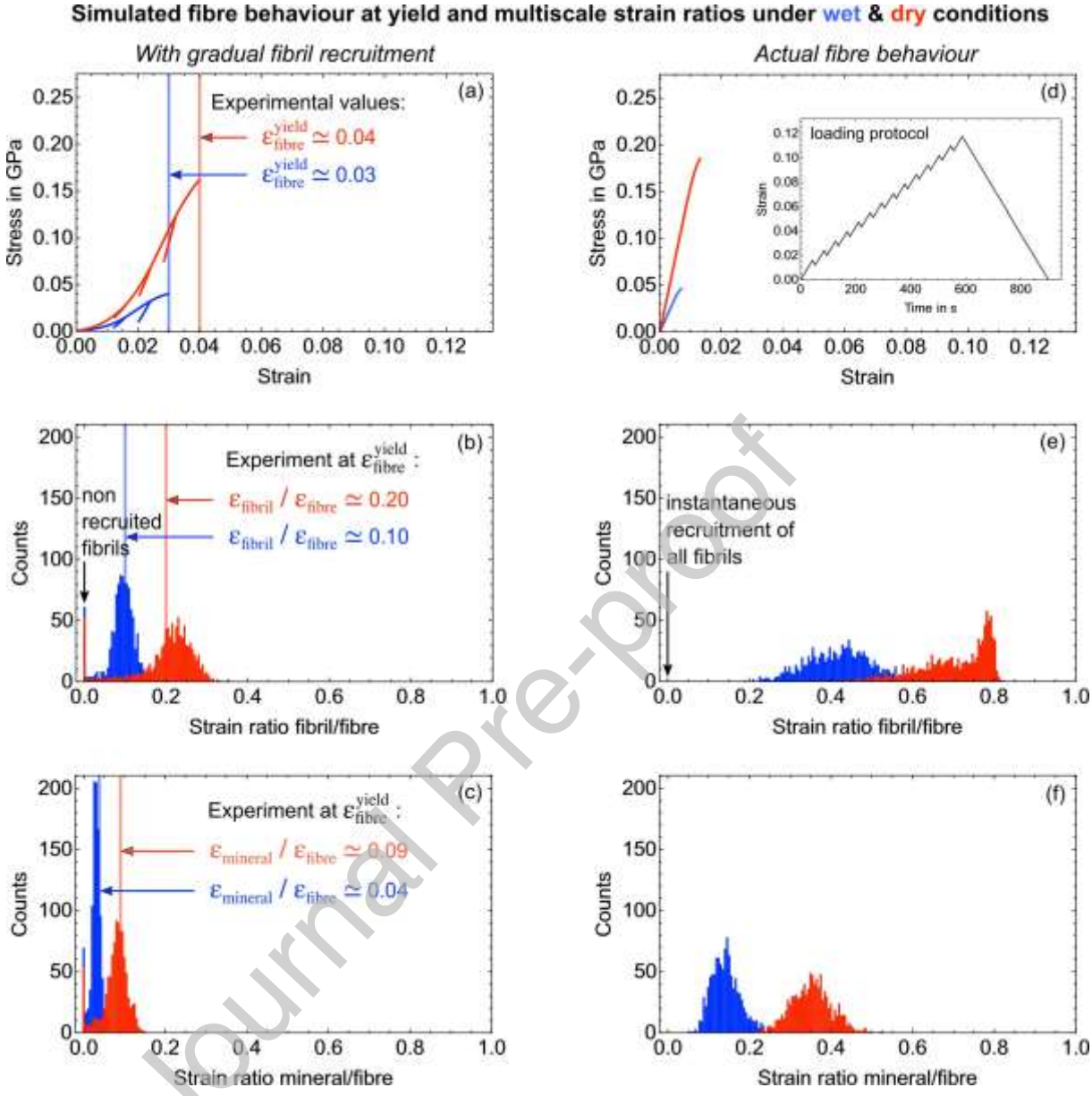

Figure 6: Model outcome for the multiscale mineralised collagen fibre behaviour as simulated at the numerical yield point for both wet and dry conditions. The top row shows the fibre stress-strain data, the second and third rows the strain ratio distributions between fibril and fibre and mineral and fibre levels. Left (a-c): Data when accounting for a gradual fibril recruitment (experimental artefact). Right (d-f): Data where the recruitment is excluded, thus depicting the actual micro- and nanomechanical behaviour of a hydrated mineralised collagen fibre. The inlay in (d) shows the loading protocol for the strain driven simulation.

excised array of fibrils. In contrast to micro-indentation tests, testing a free micropillar of an array of uniaxially arranged fibrils [21, 56] lacks the support of surrounding fibres. Since our dry testing results [56] compare well with nanoindentation [88], considering this different set of boundary conditions suggests that we observe lubrication and swelling but that this is not blocked by surrounding tissue, thus losing a reinforcing and stabilising element. This was not found in dry samples [56]. Also, the

differences between the 53:5 ratio between apparent strain and fibril strain in compression compared to 12:5 found in tension (mm sized samples) [52] might be related to the lack of supporting tissue.

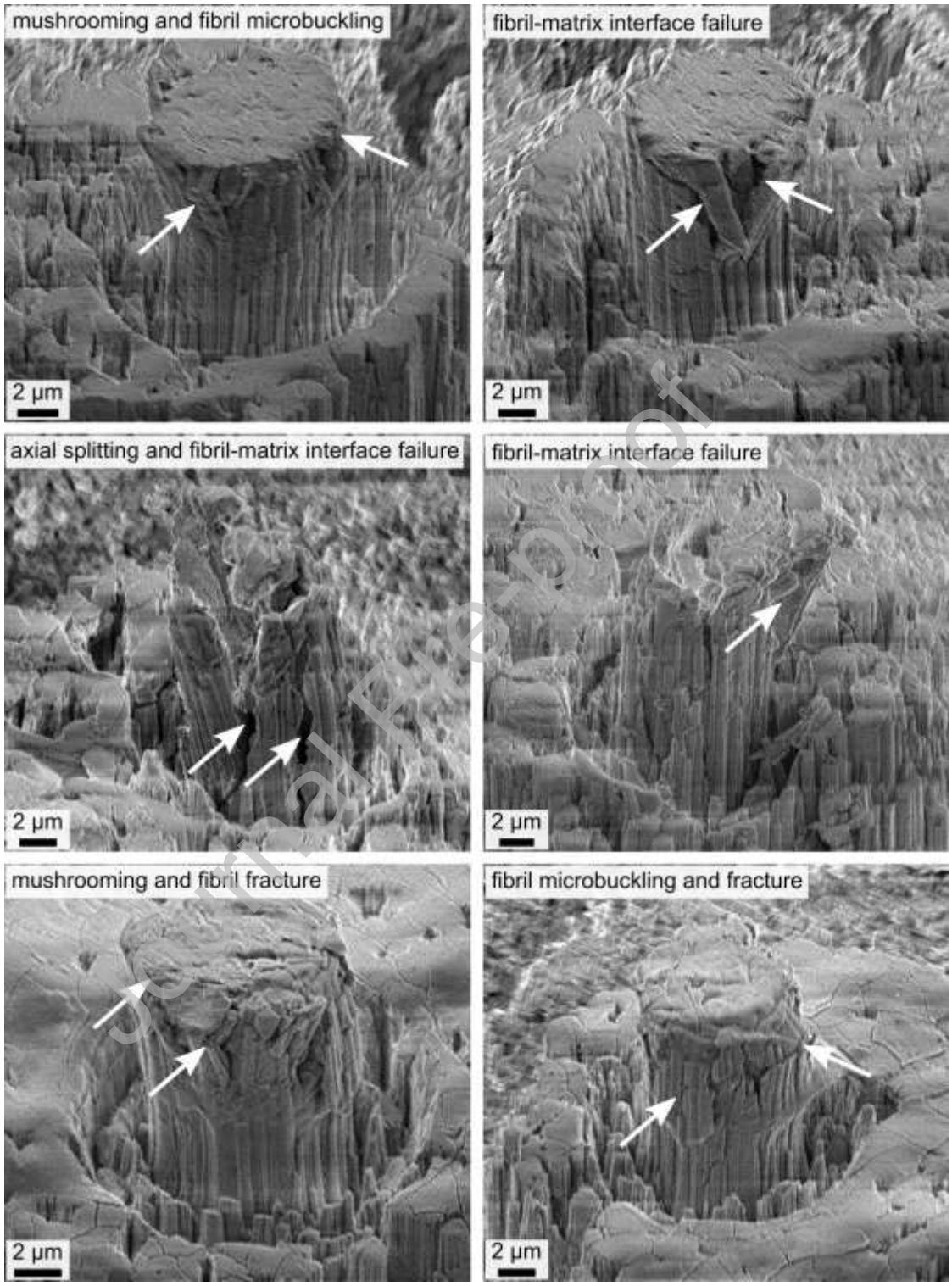

Figure 7: Failure modes of rehydrated micropillars tested under compression. Several failure modes may combine in any one specimen. For the majority of wet tested micropillars, mushrooming at the top surface was observed. In many cases, this was combined with microbuckling or fracture of mineralised collagen fibrils.

Compared to micropillar compression of rehydrated ovine cortical bone extracellular matrix [50], Young's modulus, yield stress and compressive strength are about four times lower. This can be related

to the lower mineralisation that we found in our dry samples of mineralised turkey leg tendon [21] compared to bone [89]. Generalising our statistical constitutive model towards bone extracellular matrix showed that a higher mineralisation and differences in the interfibrillar surface-to-volume ratio [21] can explain the higher compressive strength in dry bone micropillars [25]. Given that the rehydration related decrease in compressive strength is the same for bone [50] and mineralised turkey leg tendon (75%) (as observed in the present study) this effect, however, seems not to depend on the rehydration state of the tissue.

Regarding the influence of hydration on the elastic fibre behaviour we observed a decrease of stiffness between 60% and 70% compared to dry testing of the same material [56]. Our observed reduction in yield values are in line with the 65% decrease in yield properties reported for micropillar compression tests of ovine bone extracellular matrix [50]. Compared to wet and dry micro-indentation results, these values are higher where a reduction of 20-40% in the elastic modulus is reported for rehydrated ovine bone [50], 30% for rehydrated trabecular bone [48] and 6% for rehydrated mineralised turkey leg tendon [88]. Compressive tests on mm-sizes human femur samples showed a decrease in the elastic modulus of around 40% and a decrease in the compressive strength of around 55% [49]. Differences to the macroscale point towards the effect of hydration on additional interfaces when testing samples above the microscale. Our results, thus, suggest a strong influence of ultrastructural interfaces on the hydration effect, combined with the missing stabilising influence of surrounding tissue as discussed earlier. The swelling effects are also expected to be smaller at the macroscale due to a smaller surface-to-volume ratio and overall higher heterogeneity of the ultrastructure.

Studying the effect of water on the fibre constituents, we observe that the model identified a higher influence on the mineral than the fibril strain - an effect also shown for mm-sized bone samples in tension [52] and compression [49]. Compared to dry tissue [56], we observe smaller values for both the mineral and fibril strain when the fibres are wet (Figure 6). As discussed for the mineral strain, the lower strain can be explained by a lubrication of the fibrils which increased their mobility in the softer swelled up matrix when hydrated [51, 83]. This leads to rigid body movements and to a lower strain of fibrils measurable in the axial direction (see also Section 4.2).

Numerically, the effect of hydration was modelled by reducing the collagen stiffness and by using the experimentally found yield strain. The model then predicts a decrease in the apparent fibre mechanical properties including Young's modulus, yield stress and compressive strength, as seen in experiments. In general, our simulated and experimental results agree. The model also explains the fibril-to-fibre strain ratio in the elastic region as found experimentally (Figure 6). A decrease of the mineralised collagen fibril stiffness of around 25% led to a reduced apparent fibre stiffness of more than half the value under dry conditions. This decrease in the fibril Young's modulus agrees with the

15-33% decrease found in molecular dynamics simulations that investigated hydration effects on collagen fibrils deformation mechanisms [51].

4.2 Multiscale mechanical behaviour of rehydrated fibres and effect of hydration

Comparing the mineral and fibril strains, and the overall tissue strain to mm-sized compressed bone samples [49], we observe that the influence of hydration differs depending on the constituent. Compared to macroscale samples, fibrils take up 15% less strain and the mineral nearly twice as much (27%). We also see that mineral crystals take 25% less strain in relation to fibrils when directly comparing micrometre (this study) with mm-sized samples [49]. A comparison of the absolute numbers shows that the influence of water on the mineral nanocrystals is 62% higher at the micro- than the macroscale, for the mineralised collagen fibrils the corresponding value is 50%. Interestingly, when we compare the strain ratios with data on mm-sized samples in tension [52], we observe that the decrease of the apparent values is higher in micro-scale samples but the influence of hydration between the constituents is comparable. The former is most likely related to the presence of ultrastructural interfaces above the fibre level. We observe similar strain ratios between mineral nanocrystals and mineralised collagen fibrils in our MTLT micropillars (compression) compared to the mm-sized bone samples (tension) even if mineralisation is higher in bone tissue. Rationalising these comparable strain ratio values is difficult, mainly due to the different deformation behaviour in tension and compression as well as the potentially different amount of intra- and extrafibrillar mineral in both tissues. The latter is related to the fact that the embedded mineral nanocrystals within the collagenous fibrils influence the measured mineralised collagen fibril strain extracted from SAXS signals [42].

Comparing the modelling results for a mineralised collagen fibre under dry and wet conditions, and assuming that all the mineral is located within the fibrils or provided as a mineral impregnation around the fibrils (Section 4.4), we observe that the influence of hydration is 20% higher on the mineral phase than on the mineralised collagen fibrils. One could argue that applying a load directly at the level of an array of mineralised collagen fibrils, one expects a higher strain of the mineral nanocrystals, partly as a result of stress accommodation within the pore spaces between fibres when testing at higher length scales. One explanation for the smaller mineral strains, compared to both the fibril strain and the macroscale (previous paragraph), can be related to the water-mediated structuring of bone apatite [90]. The authors report that the structuring water network facilitates the stacking and orientation of apatite platelets locally. Experimental evidence was given by a higher intensity of the 002 XRD reflection (higher number of mineral platelets oriented along the main axis of the sample or their preferred orientation, respectively). Compared to X-ray tests under dry conditions [56] we also found that on average the intensity of the 002 signals is higher in wet than in dry samples. Following this rationale, the mineral nanocrystals showed a higher co-alignment in wet samples. Given the high anisotropy of the platelet shape like crystals, in turn, results in a higher overall stiffness in the mineral phase and thus a smaller mineral strain upon loading. Due to the testing at the fibre level, the effect of the water-mediated structuring on apatite is more pronounced

in our measured signals. Our data, thus, corroborate the previously reported structural data [90], and outlines the effect on the mechanical behaviour on the micro- and nanometre length scales. The effect of water on the mineralised collagen fibril strain can be related to a higher mobility of the fibrils within the glue layer of the extrafibrillar matrix as a result of a watery film around the fibrils [51] and a softer swelled up matrix environment [83]. The smaller fibril strains indicate that the interfibrillar gliding due to the watery layer has a more pronounced effect than a reduction of the collagen molecule stiffness (Figure 4). This watery layer might reduce the binding interactions between fibrils and matrix leading to a higher mobility of the fibrils within the extrafibrillar matrix. As a result, a higher amount of energy is dissipated extrafibrillar in the fibril-matrix interactions. The increased mobility might lead to a rigid body movement of the mineralised collagen fibrils within the matrix which in turn results in smaller axial fibril strains since fibrils rather move past each other than being deformed along their longitudinal direction in their uniaxial arrangement [21, 56], which affects the measured SAXS signal.

Comparing the modelling results under dry and wet conditions, the influence of hydration is roughly the same for the strain ratios between mineral nanocrystals and fibrils and those between fibrils and fibre. Assuming that the majority of mineral is located within the fibrils, this points towards three things. First, it indicates that the hydration has a more pronounced influence on the interaction between the mineralised collagen fibrils embedded in the extrafibrillar matrix compared to the intrafibrillar mechanical interaction. Second, it suggests that extrafibrillar energy dissipation mechanisms such as interfibrillar sliding, shear deformation and friction of the matrix glue layer [36, 91–93] are more subject to change during rehydration compared to intrafibrillar mechanisms such as shear strain between the collagen molecules and mineral particles, stress transfer between adjacent mineral particles and intrafibrillar sliding [61, 94, 95]. Third, it supports the suggestion that water plays an important role in the mediation of mineral-organic matrix interactions [46, 54] within the mineralised collagen fibrils.

4.3 Failure mode analysis

For the rehydrated mineralised collagen fibres, the majority of the micropillars failed by mushrooming in combination with either mineralised collagen fibril microbuckling or fracture. In most cases, an interface failure between the mineralised collagen fibril and extrafibrillar matrix was also observed. Furthermore, axial splitting occurred. The dry samples showed the formation of kink bands which led to a localised shear deformation. Axial splitting and localised shear deformation were reported for rehydrated micropillars of ovine bone extracellular matrix [50]. Mushrooming, axial splitting and localised shear deformation were further reported as failure modes for dry tested micropillars of the same material [25]. Thus, in contrast to data reported on rehydrated extracellular matrix bone samples [50], we do not observe kink bands in wet tested mineralised collagen fibres. Considering that we found kink bands in dry tested samples from the same material [56], differences in the fibril orientation might have a more pronounced effect on the failure modes under rehydrated conditions. It can be rationalised by a swelling and cushioning effect due to hydration that leads to an

elastic embedding and translates buckling into well behaved bending. As a result, the formation of kink bands is avoided. In general, kink bands in fibre-reinforced matrix composites are discussed to be a result of either microbuckling or a matrix shear failure prompted by an initial fibre misalignment [109]. The latter option is discussed as a separate failure mode where initial material imperfections are essential. Thus, for our discussion, this can mean several things. As discussed earlier, the lubrication of the fibrils increased their mobility while leading rather to a movement past each other than along their longitudinal direction, thus, reducing a potential microbuckling and subsequent formation of kink bands. As for the initial misalignment, the lamellar structure might favour the formation of kink bands in bone compared to mineralised turkey leg tendon. The presence of initial material imperfections is in general a parameter that cannot be controlled in experiments with biological tissue. Given that cross-hatched microcracks are known to occur in bone under compression, e.g. [110-112], we speculate that the ultra-lamellar setting in bone promotes the formation of these kink bands. On the other hand, the interplay between rehydration and fibrillar density may also lead to a disintegration of the uniaxial fibre reinforced composite (increased mobility) which could then prevent the build-up of the necessary shear stresses to form a kink band. Another thing we would like to add to the discussion is that mushrooming can be a form of shear band formation if the top is pushed into the pillar. The two images at the top of Figure 7 look similar to the axial splitting reported for bone [50]. This suggests that there are shear stresses acting that may be shadowed by higher mobility of the fibres due to rehydration, which then prevents more pronounced shear bands to form.

4.4 Study limitations

Our rehydration set-up avoided the potential occurrence of bubbles in fully immersed samples (Section 2.1). Preliminary tests were done to quantify the time until HBSS evaporated under ambient conditions while the diffusion state within the micropillar was estimated based on a 1D diffusion calculation (Darcy's law) [74] (Section 2.1). However, keeping the sample rehydrated before testing by using a pipette for the HBSS refill required special attention in the setup of the integrated microindenter near the X-ray tube (Figure 2). An alternative approach would be the use of a climate chamber recently reported for microscale testing where a relative humidity of up to 95% can be reached to simulate physiologically more realistic conditions regarding humidity [96]. This setup was not available for our experiments and needs to be adapted for the combined testing with X-rays. The hydration followed previously established protocols for bone samples of the same dimensions and pre-tests (see Section 2.1), but no additional on-site tests were performed. In future studies this could be added to the testing protocol. Adding water to an X-ray based experiment can lead to artefacts in the scattering/diffraction signal. However, our data were free of such parasitic scattering with the chosen parameters. Although being able to simulate the fibre behaviour, our model can only consider a single mineral phase while two are reported to be present with distinct mass fractions. Future work will be directed to this aspect. Due to limited beamtime and the complexity of the *in situ* experiments, dry and rehydrated test were performed during two synchrotron campaigns at the ESRF.

Experimental environments were kept as similar as possible to minimise influences on collected data. We operated in the same experimental hutch with no substantial beamline modifications within the one year between the two experimental campaigns. We used the same ring conditions, focussing elements and detector at ID13 as well as identical exposure times and measurement sequences. It has been reported that using X-rays leads to an irradiation influence on the material [97, 98]. In both experiments, we performed X-ray exposure tests to minimise exposure time while ensuring that we were able to record exploitable X-ray signals. We used short exposure times and kept the shutter closed for 5 s after each acquisition. In addition, we used an Eiger 4M (Dectris, Switzerland) single-photon counting detector which has high X-ray sensitivity To estimate dose *a posteriori*, we followed previously reported approaches [113-117]. We estimated dose based on the following beam, sample and experimental setup related values (see Section 2.1): Flux of $5.9 \cdot 10^{11}$ph/s at sample position (based on a gain of 10^{-3} and a diode count of 275000 counts/s at the beamlime), beam energy of 13.3 keV, mass energy-absorption coefficient at 13.3 keV of 14.6 cm^2/g for cortical bone which we interpolated linearly based on [118], beam profile of 5.5 µm x 7.0 µm. With these values, we calculated a dose of $3.24 \cdot 10^6$ Gy following [114] and $2.81 \cdot 10^6$ Gy following [113, 115-117]. This value is comparable or lower than the dose reported for single projections in SAXS tensor tomography [115] and SAXS/WAXS tensor tomography scans [116, 117]. Grünewald et al. [117] compared projections at the beginning and end of the experiment detecting no significant change within the nanostructure indicating minimal irradiation damage. Nevertheless, our dose is higher than the threshold value after which noticeable radiation damage was observed in other studies [97]. However, during our mechanical tests, we observed constant unloading moduli throughout (Section 3.1 and Figure 3). This is evidence that the material is not damaged at scales pertinent with our measurements, so that we believe the X-ray exposure minimally affected the samples. Furthermore, the irradiation relaxation tests which we performed in our first experimental session [56] (including supplementary material therein), showed no significant change in the relaxation behaviour of the tested samples, which indicates mechanical integrity throughout the test. The used flux and exposure times in our study were necessary to ensure a high enough X-ray signal intensity for analysis. In future work, a higher energy could help to reduce the absorbed number of photons and, thus, energy into the tissue.

5 Conclusion

We quantified the elasto-plastic micro- and nanoscale behaviour of rehydrated mineralised collagen fibres down to the level of mineral nanocrystals. A combined approach of *in situ* experiments and statistical model was used to quantify the fibre behaviour and effect of hydration. Stress values were more effected than strain with a 3x higher reduction in mechanical properties compared to the macroscale indicating a significant influence on ultrastructural interfaces. Lower stiffness values point towards a loss of reinforcing capacity due to missing surrounding tissue, which is more pronounced than in dry samples. Smaller fibril strains might result from a rigid body movement within the

extrafibrillar matrix, and the higher mobility within the fibril-matrix network. The hydration effect on the compressive strength for bone and mineralised turkey leg tendon was found to be comparable. This indicates that differences in mineralisation and interfibrillar surface-to-volume ratio between both mineralised tissues are independent of the rehydration state. Smaller mineral strains under wet conditions can be related to the previously reported water-mediated structuring of bone apatite. Using a constitutive model allowed us to identify changes at the molecular and fibrillar level as well as the interplay between the constitutive phases. A decrease of collagen molecule stiffness leads to a reduced fibre yield stress, compressive strength and stiffness while pointing towards differences in the intra- and extrafibrillar phases. The lack of kink bands points towards an elastic embedding of the mineralised collagen fibrils. As for dry conditions, the use of statistically variable micro- and nanoscale mechanical properties were found to be essential for the agreement with experiments. This statistical approach could be extended towards other hierarchical bio-based materials [119] or bio-material reinforced nanocomposites [120] in the future. Our findings close a gap in providing data on the compressive behaviour of single mineralised collagen fibres under rehydrated conditions. Since hydration significantly affects the micro- and nanomechanical properties of mineralised tissues, our results provide invaluable, and so far, inaccessible information on the understanding of the multiscale elasto-plastic behaviour of bone's fundamental mechanical unit while pointing towards significant differences to the macroscale.

6 Acknowledgements

This research was supported by the Engineering and Physical Sciences Research Council (EPSRC), of the
UK (grant number EP/P005756/1) and the European Synchrotron Radiation Facility (ESRF) (proposals ME-1415 and ME-1472). J.S. acknowledges funding by the Swiss National Science Foundation (SNSF) under Ambizione Grant No. 174192. We thank Dr. Richard Carter from the Institute of Photonics and Quantum Sciences at Heriot-Watt University, UK, for organising the access to the laser facilities.

References

[1] J. D. Currey. The design of mineralised hard tissues for their mechanical functions. *J Exp Biol*, 202(23):3285–3294, 1999.

[2] R. K. Nalla, J. H. Kinney, and R. O. Ritchie. Mechanistic fracture criteria for the failure of human cortical bone. *Nat Mat*, 2:164 – 168, 2003.

[3] D. Vashishth, K. E. Tanner, and W. Bonfield. Experimental validation of a microcracking-based toughening mechanism for cortical bone. *Journal of Biomechanics*, 36(1):121 – 124, 2003.

[4] J. D. Currey. Tensile yield in compact bone is determined by strain, post-yield behaviour by mineral content. *J Biomech*, 37(4):549–556, 2004.

[5] S. Weiner and H. D. Wagner. The material bone: structure-mechanical function relations. *Annu Rev Mater Sci*, 28(1):271–298, 1998.

[6] P. Fratzl and R. Weinkamer. Nature's hierarchical materials. *Prog Mater Sci*, 52(8):1263–1334, 2007.

[7] F. Rauch and F. H. Glorieux. Osteogenesis imperfecta. *The Lancet*, 363(9418):1377–85, 2004.

[8] T. van Cleynenbreugel, J. Schrooten, H. van Ooosterwyck, and J. van der Sloten. Micro-CT-based screening of biomechanical and structural properties of bone tissue engineering scaffolds. *Medical & Biological Engineering and Computing*, 44:517 – 525, 2006.

[9] M. A. Meyers, P.-Y. Chen, Y.-M. L. Albert, and S. Yasuaki. Biological materials: Structure and mechanical properties. *Progress in Materials Science*, 53(1):1 – 206, 2008.

[10] M. E. Launey, M. J. Buehler, and R. O. Ritchie. On the mechanistic origins of toughness in bone. *Annu Rev Mater Res*, 40:25–53, 2010.

[11] S. J. Hollister. 5.502 - engineering scaffold mechanical and mass transport properties. In Paul Ducheyne, editor, *Comprehensive Biomaterials*, pages 13 – 33. Elsevier, Oxford, 2011.

[12] X. Li, L. Wang, Y. Fan, Q. Feng, F.-Z. Cui, and F. Watari. Nanostructured scaffolds for bone tissue engineering. *Journal of Biomedical Materials Research Part A*, 101A(8):2424–2435, 2013.

[13] P. Varga, D. H. Pahr, S. Baumbach, and P. K. Zysset. Hr-pqct based fe analysis of the most distal radius section provides an improved prediction of colles' fracture load in vitro. *Bone*, 47(5):982– 988, 2010.

[14] E. Hamed and I. Jasiuk. Multiscale damage and strength of lamellar bone modeled by cohesive finite elements. *J Mech Behav Biomed*, 28:94–110, 2013.

[15] D. H. Pahr, J. J. Schwiedrzik, E. Dall'Ara, and P. K. Zysset. Clinical versus pre-clinical fe models for vertebral body strength predictions. *J Mech Behav Biomed*, 33:76–83, 2014.

[16] P. K. Zysset, D. Pahr, K. Engelke, H. K. Genant, M. R. McClung, D. L. Kendler, C. Recknor, M. Kinzl, J. J. Schwiedrzik, O. Museyko, A. Wang, and C. Libanati. Comparison of proximal femur and vertebral body strength improvements in the freedom trial using an alternative finite element methodology. *Bone*, 81:122 – 130, 2015.

[17] A. G. Reisinger, D. H. Pahr, and P. K. Zysset. Sensitivity analysis and parametric study of elastic properties of an unidirectional mineralized bone fibril-array using mean field methods. *Biomech Model Mechan*, 9(5):499–510, 2010.

[18] J. J. Schwiedrzik, U. Wolfram, and P. K. Zysset. A generalized anisotropic quadric yield criterion and its application to bone tissue at multiple length scales. *Biomech Model Mechan*, 12(6):1155– 1168, 2013.

[19] D. H. Pahr and P. K. Zysset. Finite element-based mechanical assessment of bone quality on the basis of in vivo images. *Current Osteoporosis Reports*, 14(6):374–385, Dec 2016.

[20] A. Speed, A. Groetsch, J. J. Schwiedrzik, and U. Wolfram. Extrafibrillar matrix yield stress and failure envelopes for mineralised collagen fibril arrays. *Journal of the Mechanical Behavior of Biomedical Materials*, 105:103563, 2020.

[21] A. Groetsch, P. K. Zysset, P. Varga, A. Pacureanu, F. Peyrin, and U. Wolfram. An experimentally informed statistical elasto-plastic mineralised collagen fibre model at the micrometre and nanometre lengthscale. *Scientific Reports*, 11(1):15539, 2021.

[22] T. J. Wess, A. P. Hammersley, L. Wess, and A. Miller. A consensus model for molecular packing of type i collagen. *Journal of Structural Biology*, 122(1):92 – 100, 1998.

[23] J. Y. Rho, L. Kuhn-Spearing, and P. Zioupos. Mechanical properties and the hierarchical structure of bone. *Med Eng Phys*, 20(2):92 – 102, 1998.

[24] G. L. Niebur, M. J. Feldstein, J. C. Yuen, T. J. Chen, and T. M. Keaveny. High-resolution finite element models with tissue strength asymmetry accurately predict failure of trabecular bone. *J Biomech*, 33(12):1575 – 1583, 2000.

[25] J. J. Schwiedrzik, R. Raghavan, A. Bürki, V. LeNader, U. Wolfram, J. Michler, and P. K. Zysset. In situ micropillar compression reveals superior strength and ductility but an absence of damage in lamellar bone. *Nature Materials*, 13(7):740 – 747, 2014.

[26] K. W. Luczynski, A. Steiger-Thirsfeld, J. Bernardi, J. Eberhardsteiner, and C. Hellmich. Extracellular bone matrix exhibits hardening elastoplasticity and more than double cortical strength: Evidence from homogeneous compression of non-tapered single micron-sized pillars welded to a rigid substrate. *J Mech Behav Biomed*, 52:51–62, 2015.

[27] U. Wolfram and J. J. Schwiedrzik. Post-yield and failure properties of cortical bone. *BoneKEy Rep*, 5:–, August 2016.

[28] J. J. Schwiedrzik and P. Zysset. An anisotropic elastic-viscoplastic damage model for bone tissue. *Biomech Model Mechan*, 12(2):201–213, 2013.

[29] N. Reznikov, R. Shahar, and S. Weiner. Bone hierarchical structure in three dimensions. *Acta Biomaterialia*, 10(9):3815 – 3826, 2014.

[30] C. Hellmich and F.-J. Ulm. Micromechanical model for ultrastructural stiffness of mineralized tissues. *J Eng Mech*, 128(8):898 – 908, 2002.

[31] W. Traub, T. Arad, and S. Weiner. Three-dimensional ordered distribution of crystals in turkey tendon collagen fibers. *PNAS*, 86(24):9822–9826, 1989.

[32] I. Jäger and P. Fratzl. Mineralized collagen fibrils: a mechanical model with a staggered arrangement of mineral particles. *Biophys J*, 79(4):1737–1746, 2000.

[33] S. Lees. A model for the distribution of hap crystallites in bone—an hypothesis. *Calcified Tissue International*, 27(1):53, Dec 1979.

[34] S. Lees, K. S. Prostak, V. K. Ingle, and K. Kjoller. The loci of mineral in turkey leg tendon as seen by atomic force microscope and electron microscopy. *Calcified Tiss Int*, 55:180–189, 1994.

[35] N. Sasaki, A. Tagami, T. Goto, M. Taniguchi, M. Nakata, and K. Hikichi. Atomic force microscopic studies on the structure of bovine femoral cortical bone at the collagen fibril-mineral level. *J Mater Sci: Mater M*, 13(3):333 – 337, 2002.

[36] T. Fantner, G. E. Hassenkam, J. H. Kindt, J. C. Weaver, H. Birkedal, L. Pechenik, J. A. Cutroni, G. A. Cidade, G. D. Stucky, D. E. Morse, and P. K. Hansma. Sacrificial bonds and hidden length dissipate energy as mineralized fibrils separate during bone fracture. *Nat Mat Let*, 4(8):612 – 616, 2005.

[37] W. Wagermaier, K. Klaushofer, and P. Fratzl. Fragility of bone material controlled by internal interfaces. *Calcified Tissue International*, 97(3):201–212, Sep 2015.

[38] L. Knott and A. J. Bailey. Collagen cross-links in mineralizing tissues: a review of their chemistry, function, and clinical relevance. *Bone*, 22(3):181–187, 1998.

[39] E. A. Zimmermann, E. Schaible, H. Bale, H. D. Barth, S. Y. Tang, P. Reichert, B. Busse, T. Alliston, J. W Ager III, and R. O. Ritchie. Age-related changes in the plasticity and toughness of human cortical bone at multiple length scales. *P Natl Acad Sci*, 108(35):14416 – 14421, 2011.

[40] A. A. Poundarik, T. Diab, m A. Sroga, G. E.and Ural, A. L. Boskey, C. M. Gundberg, and D. Vashishth. Dilatational band formation in bone. *P Natl Acad Sci*, 109(47):19178 – 19183, 2012.

[41] E. A. Zimmermann, B. Busse, and R. O. Ritchie. The fracture mechanics of human bone: Influence of disease and treatment. *BoneKey Rep*, 4(743):1 – 13, 2015.

[42] S. W. White, D. J. Hulmes, A. Miller, and P. A. Timmins. Collagen-mineral axial relationship in calcified turkey leg tendon by x-ray and neutron diffraction. *Nature*, 266:421–425, 1977.

[43] H. S. Gupta, P. Messmer, P. Roschger, S. Bernstorff, K. Klaushofer, and P. Fratzl. Synchrotron diffraction study of deformation mechanisms in mineralized tendon. *Phys Rev Lett*, 93(15):158101–1 – 158101–4, 2004.

[44] J. P. R. O. Orgel, T. C. Irving, A. Miller, and T. J. Wess. Microfibrillar structure of type i collagen in situ. *Proceedings of the National Academy of Sciences*, 103(24):9001–9005, 2006.

[45] J. D. Currey. *Bones: Structure and mechanics*. Princeton University Press, 2002.

[46] M. Granke, M. D. Does, and J. S. Nyman. The role of water compartments in the material properties of cortical bone. *Calcified Tiss Int*, 97(3):292 – 307, 2015.

[47] J. S. Nyman, A. Roy, X. Shen, R. L. Acuna, J. H. Tyler, and X. Wang. The influence of water removal on the strength and toughness of cortical bone. *J Biomech*, 39(5):931–938, 2006.

[48] U. Wolfram, H.-J. Wilke, and P. K. Zysset. Rehydration of vertebral trabecular bone: Influences on its anisotropy, its stiffness and the indentation work with a view to age, gender and vertebral

level. *Bone*, 46(2):348 – 354, 2010.

[49] J. Samuel, J.-S. Park, J. Almer, and X. Wang. Effect of water on nanomechanics of bone is different between tension and compression. *Journal of the Mechanical Behavior of Biomedical Materials*, 57:128 – 138, 2016.

[50] J. J. Schwiedrzik, A. Taylor, D. Casari, W. Wolfram, P. Zysset, and J. Michler. Nanoscale deformation mechanisms and yield properties of hydrated bone extracellular matrix. *Acta Biomaterialia*, 60:302–314, 2017.

[51] M. Fielder and A. K. Nair. Effects of hydration and mineralization on the deformation mechanisms of collagen fibrils in bone at the nanoscale. *Biomechanics and Modeling in Mechanobiology*, 18:57–68, 2018.

[52] H. S. Gupta, J. Seto, W. Wagermaier, P. Zaslansky, P. Boesecke, and P. Fratzl. Cooperative deformation of mineral and collagen in bone at the nanoscale. *P Natl Acad Sci*, 103(47):17741–17746, 2006.

[53] A. C. Deymier-Black, F. Yuan, A. Singhal, J. D. Almer, A. C. Brinson, and D. C. Dunand. Evolution of load transfer between hydroxyapatite and collagen during creep deformation of bone. *Acta Biomaterialia*, 8(1):253 – 261, 2012.

[54] E. E. Wilson, A. Awonusi, M. D. Morris, D. H. Kohn, M. M. J. Tecklenburg, and L. W. Beck. Three structural roles for water in bone observed by solid-state nmr. *Biophysical Journal*, 90(10):3722 – 3731, 2006.

[55] J. Samuel, D. Sinha, J. C.-G. Zhao, and X. Wang. Water residing in small ultrastructural spaces plays a critical role in the mechanical behavior of bone. *Bone*, 59:199 – 206, 2014.

[56] A. Groetsch, A. Gourrier, J. Schwiedrzik, M. Sztucki, R. J. Beck, J. D. Shephard, J. Michler, P. K. Zysset, and U. Wolfram. Compressive behaviour of uniaxially aligned individual mineralised collagen fibres at the micro- and nanoscale. *Acta Biomaterialia*, 89:313 – 329, 2019.

[57] M. D. Uchic, D. M. Dimiduk, J. N. Florando, and W. D. Nix. Sample dimensions influence strength and crystal plasticity. *Science*, 305(5686):986–989, 2004.

[58] D. J. Hulmes, T. J. Wess, D. J. Prockop, and P. Fratzl. Radial packing, order, and disorder in collagen fibrils. *Biophysical Journal*, 68(5):1661 – 1670, 1995.

[59] P. Fratzl, S. Schreiber, and K. Klaushofer. Bone mineralization as studied by small-angle x-ray scattering. *Connect Tiss Res*, 34(4):247 – 254., 1996.

[60] J. D. Almer and S. R. Stock. Internal strains and stresses measured in cortical bone via high-energy x-ray diffraction. *J Struct Biol*, 152(1):14–27, 2005.

[61] H. S. Gupta, W. Wagermaier, G. A. Zickler, A. D. Raz-Ben, S. S. Funari, P. Roschger, H. D. Wagner, and P. Fratzl. Nanoscale deformation mechanisms in bone. *Nano Lett*, 5(10):2108–2111, 2005.

[62] C. Burger, H. W. Zhou, H. Wang, I. Sics, B. S. Hsiao, L. Chu, B. Graham, and M. J. Glimcher. Lateral packing of mineral crystals in bone collagen fibrils. *Biophys J*, 95(4):1985 – 1992, 2008.

[63] R. Akhtar, M. R. Daymond, J. D. Almer, and P. M. Mummery. Load transfer in bovine plexiform bone determined by synchrotron x-ray diffraction. *Journal of Materials Research*, 23(2):543–550, 2008.

[64] S. Tadano and B. Giri. X-ray diffraction as a promising tool to characterize bone nanocomposites. *Science and Technology of Advanced Materials*, 12(6):064708, 2011.

[65] A. C. Deymier-Black, J. D. Almer, S. R. Stock, and D. C. Dunand. Variability in the elastic properties of bovine dentin at multiple length scales. *J Mech Behav Biomed*, 5(1):71–81, 2012.

[66] A. Bigi, A. Ripamonti, M. H. J. Koch, and N. Roveri. Calcified turkey leg tendon as structural model for bone mineralization. *Int J Biol Macromol*, 10(5):282–286, 1988.

[67] P. Fratzl, M. Groschner, G. Vogl, H. Plenk, J. Eschberger, N. Fratzl-Zelman, K. Koller, and K. Klaushofer. Mineral crystals in calcified tissues: A comparative study by saxs. *Journal of Bone and Mineral Research*, 7(3):329–334, 1992.

[68] W. J. Landis, M. J. Song, A. Leith, L. McEwen, and B. F. McEwen. Mineral and organic matrix interaction in normally calcifying tendon visualized in three dimensions by high-voltage electron microscopic tomography and graphic image reconstruction. *J Struct Biol*, 110(1):39 – 54, 1993.

[69] E. M. Spiesz, P. Roschger, and P. K. Zysset. Influence of mineralization and microporosity on tissue elasticity: Experimental and numerical investigation on mineralized turkey leg tendons. *Calcified Tiss Int*, 90(4):319–329, 2012.

[70] S. McPhee, A. Groetsch, J. D. Shephard, and U. Wolfram. Heat impact during laser ablation extraction of mineralised tissue micropillars. *Scientific Reports*, 11(1):11007, 2021.

[71] J. F. Ziegler, M. D. Ziegler, and J. P. Biersack. SRIM–The stopping and range of ions in matter (2010). *Nucl Instrum Meth B*, 268(11):1818–1823, 2010.

[72] R. K. Nalla, A. E. Porter, C. Daraio, A. M. Minor, V. Radmilovic, E. A. Stach, A. P. Tomsia, and R. O. Ritchie. Ultrastructural examination of dentin using focused ion-beam cross-sectioning and transmission electron microscopy. *Micron*, 36(7):672–680, 2005.

[73] J. Michler, K. Wasmer, S. Meier, F. Östlund, and K. Leifer. Plastic deformation of gallium arsenide micropillars under uniaxial compression at room temperature. *Appl Phys Lett*, 90(4):043123, 2007.

[74] S. P. Neuman. Theoretical derivation of darcy's law. *Acta Mechanica*, 25(3):153–170, 1977.

[75] G. van Rossum and F. L. Drake. *Python Tutorial*.

[76] R Development Core Team. *R: A Language and Environment for Statistical Computing*. R Foundation for Statistical Computing, Vienna, Austria, 2011. ISBN 3-900051-07-0.

[77] M. Ashby and D. Jones. *Engineering Materials*. Pergamon, 1980.

[78] G. A. Holzapfel. *Nonlinear Solid Mechanics: A Continuum Approach for Engineering*. John Wiley and Sons, Ltd, 2000.

[79] I. N. Sneddon. The relation between load and penetration in the axisymmetric boussinesq problem for a punch of arbitrary profile. *Int J Eng Sci*, 3(1):47–57, 1965.

[80] H. Zhang, B.E. Schuster, Q. Wei, and K.T. Ramesh. The design of accurate micro-compression experiments. *Scripta Materialia*, 54(2):181 – 186, 2006.

[81] A. P. Hammersley, S. O. Svensson, M. Hanfland, A. N. Fitch, and D. Hausermann. Twodimensional detector software: From real detector to idealised image or two-theta scan. *High Pressure Research*, 14(4-6):235–248, 1996.

[82] S. Cusack and A. Miller. Determination of the elastic constants of collagen by brillouin light scattering. *Journal of Molecular Biology*, 135(1):39 – 51, 1979.

[83] C. Morin, C. Hellmich, and P. Henits. Fibrillar structure and elasticity of hydrating collagen: A quantitative multiscale approach. *Journal of Theoretical Biology*, 317:384 – 393, 2013.

[84] R Core Team. *R: A Language and Environment for Statistical Computing*. R Foundation for Statistical Computing, Vienna, Austria, 2013.

[85] E. Jones, T. Oliphant, P. Peterson, et al. SciPy: Open source scientific tools for Python., 2001–.

[86] T. E. Oliphant. Guide to numpy, 2006.

[87] S. S. Shapiro and M. B. Wilk. An analysis of variance test for normality (complete samples). *Biometrika*, 52(3-4):591 – 611, 1965.

[88] E. M. Spiesz, P. Roschger, and P. K. Zysset. Elastic anisotropy of uniaxial mineralized collagen fibers measured using two-directional indentation. effects of hydration state and indentation depth. *J Mech Behav Biomed Mat*, 12:20–28, 2012.

[89] P. Varga, B. Hesse, M. Langer, S. Schrof, N. Männicke, H. Suhonen, A. Pacureanu, D. Pahr, F. Perin, and K. Raum. Synchrotron x-ray phase nano-tomography-based analysis of the lacunar–canalicular network morphology and its relation to the strains experienced by osteocytes in situ as predicted by case-specific finite element analysis. *Biomechanics and Modeling in Mechanobiology*, 14(2):267–282, 2015.

[90] Y. Wang, S. Von Euw, F. M. Fernandes, S. Cassaignon, M. Selmane, G. Laurent, G. PehauArnaudet, C. Coelho, L. Bonhomme-Coury, M.-M. Giraud-Guille, F. Babonneau, T. Azaïs, and N. Nassif. Water-mediated structuring of bone apatite. *Nat Mat*, 12(12):1144–1153, 2013.

[91] J. B. Thompson, J. H. Kindt, B. Drake, H. G. Hansma, D. E. Morse, and P. K. Hansma. Bone indentation recovery time correlates with bond reforming time. *Nature*, 414:773–776, 2001.

[92] H. S. Gupta, W. Wagermaier, G. A. Zickler, J. Hartmann, S. S. Funari, and P. Roschger. Fibrillar level fracture in bone beyond the yield point. *Int J Fracture*, 139:425 – 436, 2006.

[93] H. S. Gupta, P. Fratzl, M. Kerschnitzki, G. Benecke, W. Wagermaier, and H. O. Kirchner. Evidence for an elementary process in bone plasticity with an activation enthalpy of 1 eV. *J R Soc Interface*, 4(13):277 – 282, 2007.

[94] G. Benecke, M. Kerschnitzki, P. Fratzl, and H. S. Gupta. Digital image correlation shows localized deformation bands in inelastic loading of fibrolamellar bone. *Journal of Materials Research*, 24(2):421–429, 2009.

[95] H. S. Gupta, S. Krauss, M. Kerschnitzki, A. Karunaratne, J. W. C. Dunlop, A. H. Barber, P. Boesecke, S. S. Funari, and P. Fratzl. Intrafibrillar plasticity through mineral/collagen sliding is the dominant mechanism for the extreme toughness of antler bone. *JMBBM*, 28:366-382, 2013.

[96] C. Peruzzi, R. Ramachandramoorthy, A. Groetsch, D. Casari, P. Grönquist, M. Rüggeberg, J. Michler, and J. Schwiedrzik. Microscale compressive behavior of hydrated lamellar bone at high strain rates. *Acta Biomaterialia*, 131:403–414, 2021.

[97] H. D. Barth, M. E. Launey, A. A. Macdowell, J. W. Ager III, and R. O. Ritchie. On the effect of X-ray irradiation on the deformation and fracture behavior of human cortical bone. *Bone*, 46(6):1475 – 1485, 2010.

[98] E. Dall'Ara, A. J. Bodey, H. Isaksson, and G. Tozzi. A practical guide for in situ mechanical testing of musculoskeletal tissues using synchrotron tomography. *JMBBM*, 133:105297, 2022.

[99] B. Ji and H. Gao. Mechanical properties of nanostructure of biological materials. *Journal of the Mechanics and Physics of Solids*, 52(9):1963 – 1990, 2004.

[100] A. K. Nair, A. Gautieri, S.-W. Chang, and M. J. Buehler. Molecular mechanics of mineralized collagen fibrils in bone. *Nat Commun*, 4:1724, 2013.

[101] S. Tiburtius, S. Schrof, F. Molnár, P. Varga, F. Peyrin, Q. Grimal, K. Raum, and A. Gerisch. On the elastic properties of mineralized turkey leg tendon tissue: Multiscale model and experiment. *Biomech Model Mechan*, 13(5):1003–1023, 2014.

[102] E. Alizadeh, M. Dehestani, and P. Zysset. An efficient two-scale 3d fe model of the bone fibril array: comparison of anisotropic elastic properties with analytical methods and micro-sample testing. *Biomechanics and Modeling in Mechanobiology*, 2020.

[103] U. Akiva, H. D. Wagner, and S. Weiner. Modelling the three-dimensional elastic constants of parallel-fibred and lamellar bone. *Journal of Materials Science*, 33(6):1497–1509, Mar 1998.

[104] S. J. Eppell, W. Tong, J. L. Katz, L. Kuhn, and M. J. Glimcher. Shape and size of isolated bone mineralites measured using atomic force microscopy. *J Orthop Res*, 19(6):1027–1034, 2001.

[105] J. L. Katz. Hard tissue as a composite material—i. bounds on the elastic behavior. *Journal of Biomechanics*, 4(5):455 – 473, 1971.

[106] H. Yao, L. Ouyang, and W.-Y. Ching. Ab initio calculation of elastic constants of ceramic crystals. *Journal of the American Ceramic Society*, 90(10):3194–3204, 2007.

[107] F. Hang and A. H. Barber. Nano-mechanical properties of individual mineralized collagen fibrils from bone tissue. *J R Soc Interface*, 8(57):500–505, 2011.

[108] C. Mercer, M. Y. He, R. Wang, and A. G. Evans. Mechanisms governing the inelastic deformation of cortical bone and application to trabecular bone. *Acta Biomaterialia*, 2(1):59–68, 2006.

[109] S. T. Pinho, C. G. Dàvila, P. P. Camanho, L. Iannucci, P. Robinson, Failure models and criteria for frp under in-plane or three-dimensional stress states including shear non-linearity, *NASA Tech. Mem.* 213530 (18) (2005) 1–64.

[110] M. E. Arlot, Y. Jiang, H. K. Genant, J. Zhao, B. Burt-Pichat, J.-P. Rioux, P. D. Delmas and P. J. Meunier. Histomorphometric and μCT analysis of bone biopsies from postmenopausal osteoporotic women treated with strontium ranelate. *J. Bone Miner. Res.* 23(2), 215–222, 2008.

[111] D. Vashishth. Hierarchy of bone microdamage at multiple length scales. *Int. J. Fatigue* 29(6), 1024-1033, 2007.

[112] U. Wolfram, J. Schwiedrzik, M. Mirzaali, A. Bürki, P. Varga, C. Olivier, F. Peyrin and P. Zysset. Characterising loading mode dependent microcrack orientation distribution functions in osteonal bone samples. *Journal of Microscopy* 264, 268-281, 2016.

[113] M. R. Howells, T. Beetz, H. N. Chapman, C. Cui, J. M. Holton, C. J. Jacobsen, J. Kirz, E. Lima, S. Marchesini, H. Miao, D. Sayre, D. A. Shaoiro, J. C. H. Spence and D. Starodub. An assessment of the resolution limitation due to radiation-damage in X-ray diffraction microscopy. *J. Electron Spectrosc. Relat. Phenom.* 170, 4-12, 2009.

[114] A. C. Deymier-Black, J. D. Almer, S. R. Stock and D. C. Dunand. Variability in the elastic properties of bovine dentin at multiple length scales. *J Mech Behav Biomed*, 5(1), 71-81, 2012

[115] M. Liebi, M. Georgiadis, A. Menzel, P. Schneider, J. Kohlbrecher, O. Bunk and M. Guizar-Sicairos. Nanostructure surveys of macroscopic specimens by small-angle scattering tensor tomography. *Nature*, 527, pages 349-352, 2015.

[116] T. A. Grünewald, A. Johannes, N. K. Wittig, J. Palle, A. Rack, M. Burghammer and H. Birkedal. Mapping the 3D orientation of nanocrystals and nanostructures in human bone: Indications of novel structural features. *Science Advances*, 6(24), 2020

[117] T. A. Grünewald, M. Liebi, N. K. Wittig, A. Johannes, T. Sikjaer, L. Rejnmark, Z. Gao, M. Rosenthal, M. Guizar-Sicairos, H. Birkedal and M. Burghammer. Bone mineral properties and

3D orientation of human lamellar bone around cement lines and the Haversian system. *IUCrJ*, 10(2), 189-198, 2023.

[118] J. Hubbell and S. Seltzer. *Tables of X-ray mass attenuation coefficients and mass energy-absorption coefficients 1 keV to 20 MeV for elements Z=1 to 92 and 48 additional substances of dosimetric interest. Report NISTIR 5632.* National Institute of Standards and Technology, Gaithersburg, MD, USA.

[119] S. Hennige, U. Wolfram, L. Wickes, F. Murray, J. M. Roberts, N. Kamenos, S. Schofield, A. Groetsch, E. M. Spiesz, M.-E. Aubin-Tam and P. J. Etnoyer. Crumbling reefs and cold-water coral habitat loss in a future ocean: evidence of 'coralporosis' as an indicator of habitat integrity. *Frontiers in Marine Science* 7:668, 2020.

[120] A. Groetsch, S. Stelzl, Y. Nagel, T. Kochetkova, N. C. Scherrer, A. Ovsianikov, J. Michler, L. Pethö, G. Siqueira, G. Nyström and J. Schwiedrzik. Microscale 3D Printing and Tuning of Cellulose Nanocrystals Reinforced Polymer Nanocomposites. *Small* 2202470, 2022.